THESIS FOR THE DEGREE OF DOCTOR OF PHILOSOPHY

Thermal and Photon Stimulated Reactions on Metal Particles

KRISTINA WETTERGREN

Department of Applied Physics
CHALMERS UNIVERSITY OF TECHNOLOGY
Göteborg, Sweden 2014

Thermal and Photon Stimulated Reactions on Metal Particles
Kristina Wettergren
Göteborg 2014
ISBN 978-91-7597-047-9

© Kristina Wettergren, 2014.

Doktorsavhandlingar vid Chalmers tekniska högskola
Ny serie Nr 3728
ISSN 0346-718X

Department of Applied Physics
Chalmers University of Technology
SE-412 96 Göteborg
Sweden
Telephone: + 46 (0)31-772 1000

Cover: Upper Left: Part of the ultra-high-vacuum (UHV) chamber that was used for the UHV experiments presented in this thesis.
Upper Right: Schematic drawing of water clustering on a sodium atom on graphite.
Lower left: Scanning electron microscope image of an indirect nanoplasmonic sensing (INPS) chip.
Lower right: Apparent activation energy for water formation on platinum nanoparticles as a function of nanoparticle size, measured by INPS.

Chalmers reproservice
Göteborg, Sweden 2014

Thermal and Photon Stimulated Reactions on Metal Particles
Kristina Wettergren
Department of Applied Physics
Chalmers University of Technology

Abstract

The interaction between molecules and solid surfaces influence our daily lives in many ways. One important example is heterogeneous catalysis where surface reactions, for example, are used for production of chemicals and exhaust after-treatment. As surface reactions are complex, various different approaches are needed to explore the fundamental processes.

One route is to study reactions at well-defined single crystal surfaces under ultra-high vacuum (UHV) conditions. However, as the reaction pathways may depend on pressure, ideally we would like to track how and if the interactions change with pressure. Furthermore, technical catalysts generally consist of nanometre-sized particles supported by an oxide material. This introduces the complexity of particle size-dependence, as well as effects arising from interactions between the reactants and the support material.

The studies in this thesis range from fundamental studies in UHV to experiments under ambient conditions. Structure-wise, the studies encompass single crystal substrates and model catalysts. Furthermore, surface processes are stimulated by both thermal and photon energy.

The fundamental aspects of thermally driven interactions of NO and water with sodium supported on a single crystal C(0001) surface were studied in UHV. Moreover, the influence of silver particle size (and to some extent shape) on the efficiency of photon driven desorption of NO from the Ag/C(0001) system was explored.

Model catalysts were studied under ambient conditions by use of indirect nanoplasmonic sensing (INPS). In particular, INPS was used to determine the apparent activation energy for hydrogen oxidation as a function of platinum nanoparticle size, and to track the sintering of platinum clusters.

Keywords: Nitric Oxide, Water, Sodium, Graphite, Plasmons, Silver Nanoparticles, Photodesorption, Platinum Nanoparticles, Hydrogen Oxidation, Platinum Clusters, Sintering

Appended Papers

The thesis is based on the following papers:

I. **Co-adsorption and reaction of Na and H_2O on graphite**
M. A. Gleeson, K. Mårtensson*, B. Kasemo, and D. V. Chakarov
Applied Surface Science, 235, 91-96, 2004.

II. **The interactions of Na, NO, and H_2O on the graphite (0001) surface**
M. A. Gleeson, K. Mårtensson*, B. Kasemo, D. V. Chakarov, R. Reibke, and E. Hasselbrink
Journal of Chemical Physics, 119, 6753-6767, 2003.

III. **Photodesorption of NO from graphite (0001) surface mediated by silver clusters**
K. Wettergren, B. Kasemo, and D. V. Chakarov
Surface Science, 593, 235-241, 2005.

IV. **Unravelling the Dependence of Hydrogen Oxidation Kinetics on the Size of Pt Nanoparticles by *in operando* Nanoplasmonic Temperature Sensing and DFT Calculations**
K. Wettergren, A. Hellman, F. Cavalca, A. Trinchero, H. Grönbeck, V. P. Zhdanov, and C. Langhammer
In Manuscript.

V. **High Sintering Resistance of Size-Selected Platinum Cluster Catalysts by Suppressed Ostwald Ripening**
K. Wettergren, F. F. Schweinberger, D. Deiana, C. J. Ridge, A. S. Crampton, M. D. Rötzer, T. W. Hansen, V. P. Zhdanov, U. Heiz, and C. Langhammer
Submitted to Nano Letters.

*My last name used to be Mårtensson.

My Contributions to the Appended Papers

I. I performed control experiments and took part in the writing of the paper.

II. I performed part of the measurements and took part in the writing of the paper.

III. I conducted the photodesorption and NO-adsorption/desorption measurements and analysed the corresponding data. I wrote the first draft of the paper.

IV. I made the samples for the indirect nanoplasmonic sensing (INPS) measurements. I conducted the INPS-measurements, analysed the INPS-data, and wrote the first draft of the manuscript.

V. I made the INPS-substrates, performed the INPS-measurements and analysed the data. I wrote the first draft of the manuscript together with C. Langhammer.

Contents

Chapter 1

Introduction

The interaction between molecules and solid surfaces is a fundamental process that affects our daily lives in many ways. One striking and visible example is the corrosion of copper roofs and drains, giving them the green colour we all associate with older buildings. In fact, many surfaces are covered by molecules, and a clean metal surface at atmospheric pressures will be covered by oxygen in less than a μs. An important application of molecule/surface interactions is heterogeneous catalysis, i.e. processes where the activation barrier (energy cost) for a desired process is lowered by the presence of a catalyst surface. Catalysis provides us with approximately 85-90% [1] of the chemicals produced by the chemical industry and it is the process enabling exhaust cleaning in vehicles (platinum catalyses, for example, the oxidation of CO to CO_2), as well as the mechanism behind the processes in hydrogen based energy systems. A route to further improving the activity and selectivity of catalysts, and surface processes in general, is to understand the fundamental processes.

One approach to gain understanding of the complex processes taking place at surfaces under ambient conditions is to study the different elementary processes that are involved on clean, microscopically well-defined surfaces. The combination of single-crystal surfaces and ultra-high-vacuum (UHV) systems (pressure $\sim 10^{-10}$ torr) gives a well-defined, clean surface and an environment where different spectroscopic methods can be used to probe i) the surface itself, ii) adsorbate-surface and adsorbate-adsorbate interactions, and iii) reaction products leaving the surface. The need for these kinds of systems was one important driving force behind the evolution of surface science in the 1960's.

It is, however, not always possible to extrapolate the results from surface science studies to the more complex systems under ambient pressure. For example, catalytic reactions might follow different routes depending on the

reactant pressure. The trend today is, therefore, to develop spectroscopic techniques that can be used at pressures as close to real application conditions as possible. Ideally, we would like to be able to follow if and how the interactions change when the pressure is increased. This is often referred to as bridging the pressure gap. Recent developments along this path include environmental transmission electron microscopy (ETEM), high-pressure X-ray photoelectron spectroscopy, and nanoplasmonic sensing.

Another complication arises from the fact that most surfaces that are involved in processes under ambient pressure are far from single-crystalline. As catalysis is a surface process, one would like to maximise the surface/volume ratio and in applied catalysis, the active phase is often small, nanometre-sized, particles. The use of nanoparticles is a way to minimise the cost of the catalyst by minimising the total amount of active (expensive, e.g. platinum) material. The metal particles are generally supported on an oxide surface, thereby introducing another material that may interact with the molecules and affect the catalytic process, e.g. by spill-over steps or metal-support interactions. The difference in structure between single-crystal surfaces and supported particles has been termed the materials gap.

To overcome the materials gap, model systems of the catalysts are usually employed. Nanofabrication methods have made it possible to make model systems of supported particles with a great degree of control over both size and shape of the supported particles. This makes it possible to design the properties of the model system by changing the size of the particles. Nanoparticles that are smaller than $\sim$5 nm have properties that scale with the nanoparticle size, whereas the properties of very small particles (clusters, $<$100 atoms) vary in a non-scalable way. In principle, this gives the opportunity to tailor the system to the desired performance. In practice, however, the small supported particles are prone to sintering (growth of mean particle size) over time, leading to deactivation of the catalyst as well as loss of the size-specific properties.

To allow for reactions to occur, energy barriers have to be climbed, thus energy has to be deposited into the system. The most common such driving energy is the heat bath, i.e. the thermal energy of the system. There are, however, also non-thermal ways of depositing energy. Exposing the sample to energetic electrons or energetic light are other ways of transferring energy to the system. The advantages of providing the energy by electron or photon irradiation is that one can select the exact energy to be transferred, and it also enables the transfer of energies (several eV) that are out of reach in the heating case. In the case of excitation via photon irradiation, advantage can be taken of the fact that metal particles have size- and shape-dependent optical resonances (e.g. plasmons) that can be utilized to transfer the desired

amount of energy to the system. The combination of irradiation (∼solar intensity light) of plasmonic structures with thermal energy has been shown to lower the operating temperature in some catalytic reactions [2].

The studies in this thesis range from fundamental studies in UHV to experiments under ambient conditions. Structure-wise, the studies encompass single crystal substrate to model catalysts, and in terms of energy transfer, both thermal and photon energy have been used to drive the processes of interest.

Papers I-II explore the fundamental aspects of thermally driven interactions of NO and water with sodium supported on a single crystal C(0001) surface in UHV. In Paper III, the influence of silver particle size (and to some extent shape) on the efficiency of photon driven desorption of NO from the Ag/C(0001) system was investigated.

Model catalysts were studied under ambient conditions by use of indirect nanoplasmonic sensing (INPS). In Paper IV, INPS was used to determine the apparent activation energy for hydrogen oxidation as a function of platinum nanoparticle size, whereas in Paper V, INPS was used to track the sintering of platinum clusters on a Si_3N_4 support.

This thesis begins with a general presentation of surface properties and surface processes in Chapter 2. The background for the studies involving coadsorption systems on graphite, i.e. Papers I-III, is then provided in Chapter 3. In Chapter 4, platinum as a surface and its interaction with H_2 and O_2, both separately and when coadsorbed, are presented. This provides the background for the study in Paper IV. The optical response of supported metallic nanoparticles is described in Chapter 5, with focus on photon induced surface processes and sensing applications. The used experimental setups and techniques are presented in Chapter 6. The main results in the appended papers are summarised in Chapter 7, followed by concluding remarks (Chapter 8) and acknowledgements (Chapter 9).

Chapter 2

Surfaces and Surface Processes

THE aim of this chapter is to introduce basic properties of solid surfaces and the fundamental processes that occur when atoms and molecules interact with surfaces. Unless other references are given, this account is based on the presentation by Zangwill [3]. The intention is to give a general background, but strongly biased towards what is relevant for the studies presented in this thesis.

2.1 Single Crystal Surfaces

THE structure of the bulk of a solid is organised so as to minimise Gibbs free energy. In many cases this leads to close-packed structures. This is the origin of the crystal structure of the bulk. At the surface, however, some of the bonds that are present in the bulk are missing. In platinum (Pt), for example, the number of nearest neighbours in the bulk is twelve, while it is nine at the stable Pt(111) surface. These missing bonds are usually referred to as "dangling bonds". The presence of dangling bonds results in an energy penalty which can be reduced by surface reconstruction. The reconstruction can be slight or, in some cases, dramatic with respect to the terminated bulk structure. The degree of reconstruction depends on both the nature of the bonding in the material and the orientation of the surface. For example, for a silicon surface along the 100 crystal direction, the reconstruction results in a new unit cell, which is twice the bulk unit cell in one lateral dimension [4]. This surface is denoted Si(100)2x1, see Figure 2.1.

Not all surfaces reconstruct, several surfaces maintain the bulk structure and the only difference compared to the terminated bulk is a relaxation of the interlayer distance [5]. This relaxation can be either a contraction or an expansion.

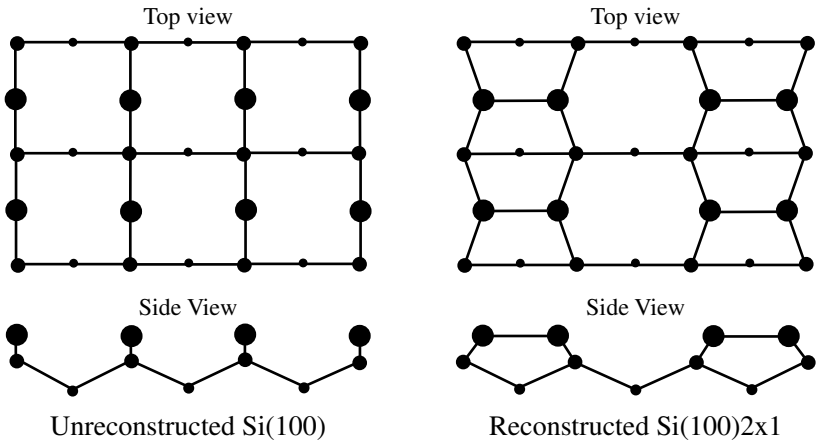

Figure 2.1: The reconstruction of the Si(100) surface (right). The unreconstructed surface is shown for comparison (left). The sizes of the silicon atoms decrease away from the page. Adapted from [6].

A perfect surface has (just as the bulk) a lateral repetition of the surface unit cell along the surface plane. This limits the possible adsorption geometries with high symmetry for atoms and molecules to a set of specific adsorption sites. Examples of such sites are on top of one of the surface atoms (ontop site), in between two surface atoms (bridge site), and inside a ring of x surface atoms (x-fold hollow site). There are two different types of three-fold hollow sites on a (111)-surface; hcp-hollow, which has one atom directly under the hollow site, and fcc-hollow which does not have an atom directly below the hollow site. Each of these adsorption sites presents a different environment and the preferred site depends on the details of the bonding of the adsorbate to the surface. Due to adsorbate-adsorbate interaction, the preferred adsorption site may also change as the coverage changes. Adsorption of atoms or molecules can, furthermore, induce surface reconstruction, because a new chemical situation is established. If, for example, the adsorbate layer saturates dangling bonds, it may remove a reconstruction that was energetically favourable for the clean surface. One example is the lifting of the reconstruction upon adsorption of ethene on Pt(100) [7]. Before adsorption, the surface atoms are reconstructed to a hexagonal structure that is rotated 0.7°, with respect to the substrate (Pt(100)-hex-R0.7°).

The adsorption sites and their bond strengths may differ between different surfaces. This is one reason why different surfaces of the same solid may show different reactivities.

2.2 Finite Systems

FINITE systems in this context refers to *nanoparticles* and *clusters*. Nanoparticles are particles where the relevant length scale (diameter for spherical nanoparticles) is less than one μm, whereas the term clusters is used here to describe systems with less than a couple of hundred atoms.

If the nanoparticles are large enough, the equilibrium shape (at 0 K) can be calculated using the Wulff theorem [8]:

$$\frac{\gamma_i}{h_i} = constant, \tag{2.1}$$

where γ_i is the surface energy of facet i, and h_i is the distance from the centre of the nanoparticle to that facet. For platinum and other fcc metals, this results in truncated octahedrons exhibiting (100) and (111) facets (terraces), as shown in Figure 2.2. As the particle shrinks, the ratio of edge and corner atoms to terrace atoms increases. These atoms have a lower coordination number (fewer nearest neighbours) than the terrace atoms, rendering them less stable, as well as more prone to form bonds with adsorbates [9]. In general, edge and corner sites have higher binding and lower dissociation energies for adsorbates than the terrace sites [10].

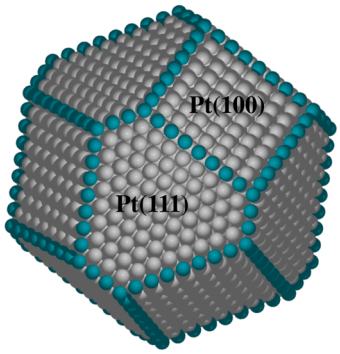

Figure 2.2: Wulff construction for a platinum nanoparticle [11]. The surface energies for Pt(111) and Pt(100) are 0.143 and 0.171 eV/Å^2, respectively [12].

It should be noted that the structural motif may change as the particles become smaller. One example is the existence of structures with five-fold symmetries for gold particles below ∼2 nm [13]. For small clusters, their shape will go from two-dimensional (for the clusters with few atoms) to three-dimensional (tending to spherical configurations) for larger sizes. At which size the cross-over from two- to three-dimensional occurs depends on

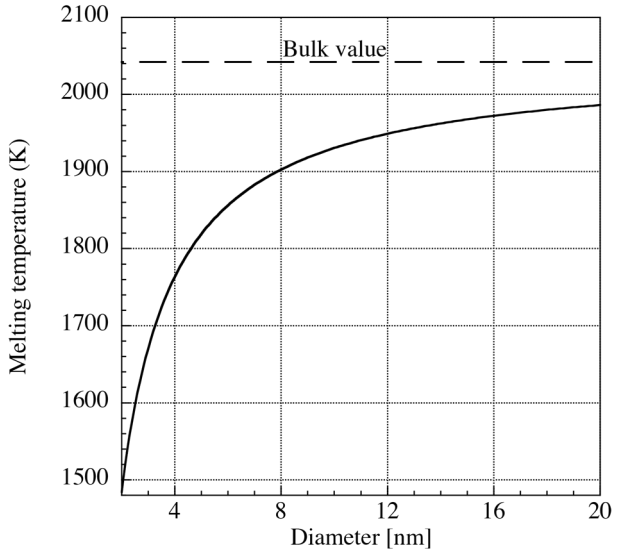

Figure 2.3: Melting temperature of platinum nanoparticles as a function of particle diameter. The curve was calculated using the Gibbs-Thomson relation, $T_m(d) = T_m(bulk)x\left(1 - \frac{4\gamma_{sl}}{\Delta H_f \rho_s d}\right)$ [17]. The values for the bulk melting temperature, $T_m(bulk)$, the heat of fusion, ΔH_f, and the solid density, ρ_s were taken from [18]. The value of the interfacial energy between solid and liquid, γ_{sl}, was taken from [19].

the element [14, 15]. For small clusters, there can be several *isomers*, i.e. different configurations, for the same number of atoms [16].

As surface atoms have a lower coordination number than the bulk atoms, and as the fraction of surface (i.e. terrace, edge and corner) to bulk atoms increases when particles become smaller, it is clear that properties of nanoparticles that are connected to the stability of the atoms will change from the corresponding bulk value [9]. One example is the melting temperature, which will decrease with decreasing particle size. The decrease in melting temperature (calculated using the Gibbs-Thomson relation [17]) with decreasing particle diameter for platinum nanoparticles is shown in Figure 2.3.

The electronic structure of the clusters will be determined by the number of atoms in the cluster, as well as how many electrons each atom donates to the delocalised state. For free electron clusters, this results in so-called "magic numbers". Sizes with enhanced stability are clusters with 8, 20, and 34 atoms, where each atom donates one electron to delocalised states [9].

2.3 Adsorption

FIGURE 2.4 is a schematic picture of adsorption, desorption and diffusion, all of which are important processes with respect to chemical reactions at surfaces. They will be described in detail in this and the following sections, starting with adsorption. *Adsorption* is the process where impinging atoms or molecules form bonds to the surface. The binding of atoms and molecules (adsorbates) to the surface (substrate) may occur by different types of bonds, which are commonly divided into either the weak bonding of van der Waals type, *physisorption*, or by formation of chemical bonds between the adsorbates and the substrate, *chemisorption*. The chemisorption bond may have ionic, covalent or metallic character. With respect to bond-strengths, there is no distinct boundary between physisorption and chemisorption, but more of a gradual change from weak to strong interaction.

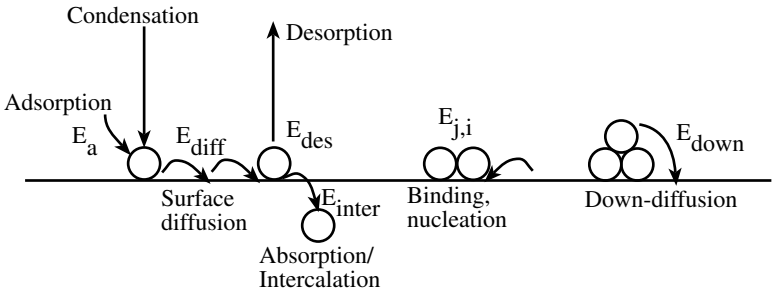

Figure 2.4: A schematic picture of the different surface processes that are described in Sections 2.3-2.5.

The interaction between an adsorbate and a solid surface can be described by the potential energy experienced by the gas particle as it approaches the surface, the solid line in Figure 2.5. This potential energy consists of two components, one repulsive part, the dotted line in Figure 2.5, which is due to the overlap of the adsorbate and surface orbitals at short distance (Pauli repulsion), and one attractive part, the dashed line in Figure 2.5, which originates from long-range forces as e.g. the van der Waals force.

Close to the surface, the potential energy also depends on which site the gas particle approaches, and in the case of molecules, also on their orientation relative to the surface. The first model of this was proposed by Lennard-Jones and describes the interaction between closed shell-atoms. A representation of the simple case where the adsorbate is an atom or a molecule with fixed molecular coordinates, is shown in Figure 2.5. The energy gained by the formation of the substrate-adsorbate bond is given by the depth of the adsorption well, E_a. Since the surface potential energy is modified by the

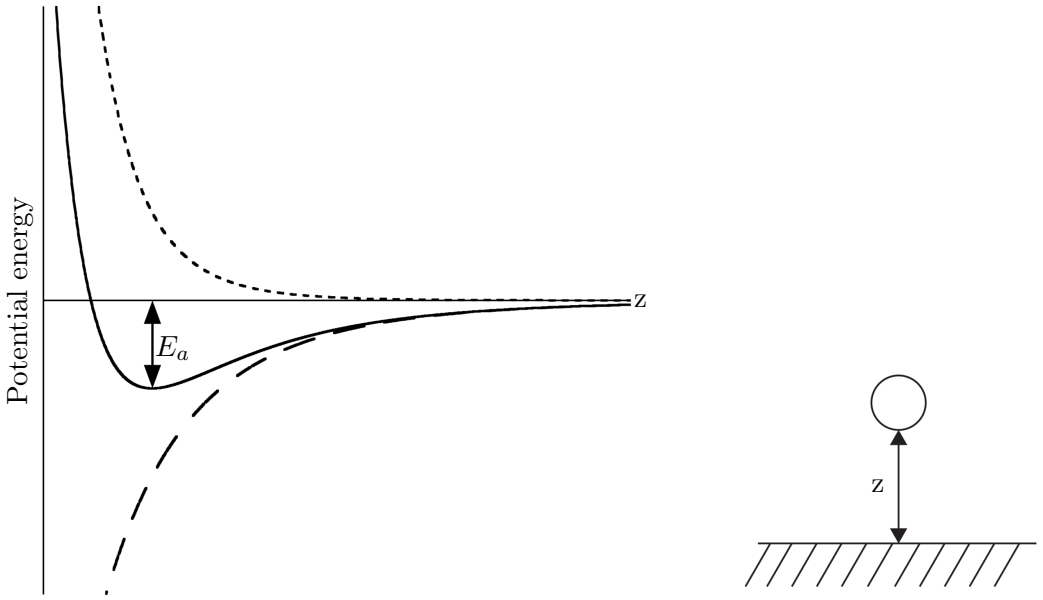

Figure 2.5: Example of the potential energy experienced by the incoming gas particle. The z-axis shows the distance between the atom or molecule and the surface. The zero of energy is taken as the energy of the gas particle at an infinite distance from the surface. This type of graph is usually referred to as a potential energy curve.

adsorbates, this value depends on the coverage. For physisorption, E_a is typically less than 0.3 eV, due to the weak interaction responsible for the bond formation. The low binding energy is the reason why physisorption usually is studied at low temperatures. This can be understood by considering the fact that the time spent at the surface by an adsorbate (the residence time, τ) is given by:

$$\tau = \tau_0 \times e^{\left(\frac{E_a}{kT}\right)}, \tag{2.2}$$

where τ_0 is the typical period of vibration along the surface-adsorbate bond. Typically, τ_0 is in the order of picoseconds. For a physisorbed adsorbate at room temperature (T=300 K) and with E_a=0.3 eV, the residence time will be of the order of 0.1 μs, whereas at T=100 K it will be approximately 1000 seconds. Therefore, physisorption is usually studied at substrate temperatures below 100 K. However, even at higher temperatures, physisorption may occur and it can be of importance as, for example, a precursor state to chemisorption.

For chemisorption, the nature and strength of the bond is determined by the interaction between the valence electrons of the adsorbate and the surface. For the solid, these are the Bloch states and for the adsorbate

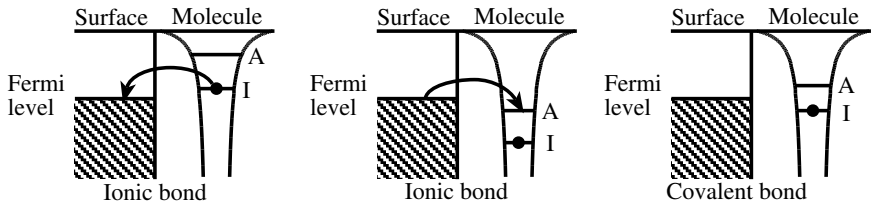

Figure 2.6: The three possible situations for neutral atoms binding to a metal surface. The affinity level, A, is unoccupied and the ionisation level, I, is occupied in the gas phase.

it is the atomic or molecular orbitals. When adsorbate and surface states interact, they hybridise and form new electron states that lower the energy of the combined adsorbate-substrate system. Thus, the detailed interaction depends on the electron structure of both the substrate and the adsorbates. Typical chemisorption energies are in the range 1-10 eV.

In the case of adsorption on metal surfaces, an important factor for the bond type is the relative position of the Fermi level of the substrate to the ionisation and affinity levels of the atom. Three possible scenarios are shown in Figure 2.6. If the ionisation (affinity) level of the adsorbate lies above (below) the Fermi level the adsorbate donates (accepts) electrons to (from) the surface. Both cases result in an essentially ionic bond being formed between adsorbate and substrate. If the Fermi level lies in between the ionisation and affinity levels, electrons will be shared by the adsorbate and substrate and the result has more of a covalent bond character. The charge transfer that is involved in the ionic bonding affects the electronic configuration of the metal substrate. In the simplest cases (ignoring diffusion of adsorbates into the bulk), the result is a lowered work function value if the adsorbates are electron donors (as for example alkali metals) and an increased work function if the adsorbates are electron acceptors (for example O or O_2).

Electron transfer into antibonding orbitals of adsorbed molecules may cause dissociation (breaking) of the molecule during the adsorption. This phenomenon is called dissociative adsorption. The dissociation is not necessarily barrierless, it may instead be an activated process as depicted in Figure 2.7. The molecule is in this case adsorbed in the precursor state and only if the energy is high enough it will overcome the barrier and dissociate.

A surface that is kept at constant temperature and exposed to a constant gas pressure will acquire an adsorbate layer that is in thermal equilibrium with the gas, i.e. the rates of adsorption and desorption will be equal. The amount of adsorbates in this layer (=the coverage, θ) will be constant and, thus, not vary over time. The coverage depends on the adsorption energy, the

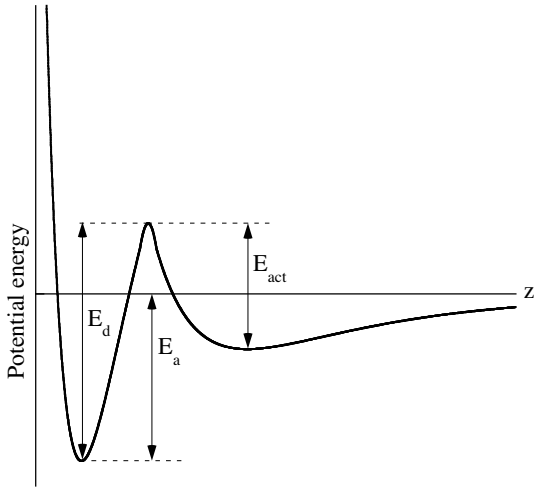

Figure 2.7: The potential energy curve for activated dissociation. The activation barrier is given by E_{act}, the adsorption energy by E_a and the desorption energy by E_d. The z-axis shows the distance between the molecule and the surface.

gas pressure and the temperature. Individual particles leave or adsorb on the surface at this adsorption-desorption equilibrium. If the pressure is suddenly reduced to zero, there is no adsorption and the adsorbed particles desorb until the surface coverage is zero. By measurements of the adsorption-desorption equilibrium coverages for a range of pressure and temperature combinations, it is possible to determine the coverage dependent binding energies.

If the combination of adsorption energy (being relatively high) and temperature (being sufficiently low) is such that no desorption occurs on the experimental time scale, the surface will eventually be saturated by adsorbate molecules. The pressure can in this case be reduced to zero and the saturated adsorption layer is still maintained. This situation is commonly used for various spectroscopic and kinetic studies of adsorbate layers. It was, for example, used in Papers I-III to co-adsorb different species on a graphite surface. Moreover, by interrupting the gas exposure time, lower coverages can be established.

The incoming flux, Φ, of particles (atoms or molecules) at a surface exposed to a gas pressure, P, is given by [18]:

$$\Phi = \frac{P}{\sqrt{2\pi m k T_g}}, \tag{2.3}$$

where m is the mass of the gas particle, and T_g the temperature of the gas. The path the adsorption system follows towards the equilibrium coverage de-

pends on the specific properties of the substrate and the impinging particles, as well as on the incident angle of the particles. If, as is the case for the experimental studies in Papers I-III, the translational and internal energies of the gas particles are fixed (fixed T_g) for all adsorption experiments and the direction is likewise fixed, the amount of particles that adsorb per unit time will depend on the particle coverage, θ, at the surface, due to the diminishing number of adsorption sites with increasing coverage.

The macroscopic behaviour of the adsorption is described by the sticking coefficient, $S(\theta, T_s)$, which is defined as the fraction of the impinging particles (per unit time) that sticks to the surface. One way to determine the variation of the sticking coefficient with coverage, is through uptake (coverage) curves. An uptake curve is a plot of the coverage as a function of the gas dose/exposure (measured e.g. in Langmuirs, 1 L=10^{-6} torr×s) at a fixed temperature. From the uptake curves, $S(\theta)$ is obtained by determining the slope of the curve for each value of θ. The initial sticking coefficient, S_0, is also determined from these curves (at θ=0). S_0 is strongly affected by even a small number of surface defects, which leads to a large variation in the reported values for the same adsorption system. This is, however, not the case when the sticking coefficient is high (near unity) for both "normal"and defect sites. For adsorption systems where multilayer adsorption does not occur, $S(\theta)$ will be zero once the saturation coverage has been reached. This saturation coverage is sometimes defined as one monolayer (ML). This is, however, an ambiguous definition, as one monolayer quite frequently refers to the number of substrate atoms at the surface, and the saturation coverage is usually only a fraction of this number.

Apart from adsorbing, the impinging particles could also be temporarily trapped at the surface (we are here talking about sub-second time scales), i.e. be unable to move away from the surface but still not be irreversibly bound to the surface. The time spent at the surface in a trapped state is much shorter than the time spent in a bound state and the species is not pinned to a certain site. The process is important for weakly bound species and for the formation of precursor states to strongly bound species.

2.4 Desorption

The inverse process to adsorption is called *desorption*. It is a process that requires energy to break the substrate-adsorbate bond. The energy can be supplied by vibrational or electronic excitations. Vibrational excitation is usually mediated by phonons (thermal excitations in the substrate), whereas electronic excitations can be due to electronic substrate excitations (usually

due to incoming electrons or photons), or sometimes direct excitations of the adsorbate by e.g. photons or electrons. The mechanisms behind electron and photon driven desorption will be presented in Section 2.7 and therefore only the thermally driven desorption is discussed here.

Thermally driven desorption is due to vibrational energy exchange between the substrate (phonons) and the adsorbate (vibrations along the substrate-adsorbate bond). In principle, there are also thermal electronic (primarily electron-hole pair) excitations but they have in most cases too low energy to play a significant role, so they are not included in this discussion.

When the substrate and the adsorbate are in thermal equilibrium, the number of phonons with energy E is $\propto e^{\frac{-E}{kT_s}}$, with T_s being the surface temperature. Likewise, the number of adsorbates that are vibrationally excited into state i (having energy ϵ_i) is $\propto e^{\frac{-\epsilon_i}{kT_s}}$. Therefore, it is possible for a single phonon having $E < E_d$ to induce desorption. Increasing the substrate temperature, will lead to a higher population of the vibrationally excited states for the adsorbates, as well as an increased number of high energy phonons. For sufficiently excited adsorbed molecules, vibrational energy can be transferred from the internal molecular vibrations to the substrate-adsorbate bond, and lead to desorption of the molecule. Since the molecular vibrations have comparatively low energy, this type of energy transfer is only possible in the case of rather highly vibrationally excited adsorbates. This is due to the narrowing spacing of the vibrational energy levels with increasing energy, as the continuum (i.e. a free gas phase species) is approached, see Figure 2.8. It is also possible to have multi-phonon induced desorption processes, where one either has simultaneous absorption of many phonons by the adsorbate-substrate bond, or the adsorbate is excited from the initial vibrational state to a higher one by one phonon, followed by another phonon excitation, and so on until desorption occurs.

As the adsorption energy is influenced by the adsorbate-adsorbate interaction, the desorption energy will also be influenced by that interaction. For non-interacting adsorbates, the desorption rate will be proportional to the coverage. For associative desorption (the inverse process to dissociative adsorption) the desorption rate will, in the simplest case of non-interacting adsorbates, have a quadratic dependence on the coverage. If, on the other hand, the adsorbates are condensed in multilayers on the substrate, so that the desorption of one adsorbate leaves the system unperturbed, the desorption rate is independent of the coverage. There are, of course, exceptions to the general cases outlined above, one being associative desorption of island-forming adsorbates. In that case, the desorption rate is proportional to the coverage, i.e. first order, instead of having the expected quadratic coverage-dependence.

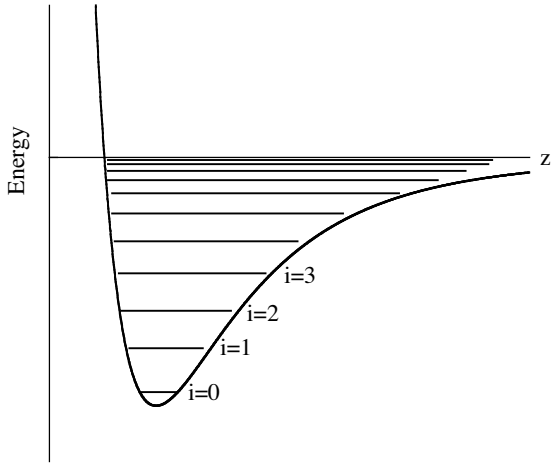

Figure 2.8: Schematic picture of the vibrational states of the adsorbate-substrate bond.

2.5 Diffusion

Even if the transferred vibrational energy from the substrate to the adsorbate is less than needed to stimulate the desorption process, it does not necessarily mean that the adsorbate remains at the same location at the surface as before the energy transfer takes place. Lateral motion, *diffusion*, can take place if the transferred energy is sufficient to overcome the energy barrier, E_{diff}, for diffusion. The barrier height will depend on the initial position of the adsorbate on the surface, as well as the attempted direction. This is due to the differences in local electronic density along the different directions of the surface. Since typically E_{diff} ~5-20% of the desorption energy, diffusion takes place even at temperatures where desorption is negligible. One example of this is the self-diffusion of rhodium atoms on Rh(111), which takes place already at ~50 K [20].

Other thermally activated processes are *absorption*, where adsorbates diffuse into the substrate, and the reverse process, *segregation*, where atoms move from the interior of the substrate to the adsorbate layer at the surface. A special case is when this occurs with layered substrates, such as graphite. The motion from the adsorbate layer into the space between the atomic layers in the layered material is called *intercalation*. All alkali metals except sodium have been shown to readily intercalate in graphite, see Section 3.2 [21, 22]. In the alkali/graphite case, the energy barriers for the intercalation process is similar to the energy barriers for desorption, which means that the two processes will compete. However, the exact values for the intercalation barrier is, in practice, also strongly influenced by the presence of defects.

2.6 Surface Reactions

SURFACE reactions differ from gas phase reactions in three main ways. First of all, the molecules on the surface are, on the average, much closer together than when in gas-phase (the average molecule-molecule distances on the surface are in the order of Ångströms). The mean free path, l, for collisions between molecules in the gas phase is $l = \frac{k_b T}{\pi\sqrt{2}d^2 P}$, with d being the size of the molecules, T the temperature, and P the pressure of the gas. For gases at room temperature and atmospheric pressures, the mean free path is about 100 nm. Secondly, the molecule-surface interaction modifies the electronic and vibrational states of the molecule, see Section 2.3, which in some cases can be favourable for reaction. Thirdly, the adsorbed molecules are aligned with respect to each other and the surface, making some bonds and rearrangements more probable. In addition, the combined momentum and energy conservation rules are much more restrictive for gas phase reactions, especially for two-body reactions. For surface reactions, the substrate acts as an efficient momentum and energy absorber (or supplier at higher temperatures). One example of this is the adsorption of molecular oxygen on metal surfaces, where oxygen goes from being in a triplet state in the gas phase, while the dissociated molecule is a singlet.

All the differences listed above can make it easier to obtain reactions on the surface as compared to having the molecules in the gas-phase. The modified electronic structure together with the alignment of the adsorbates might provide new reaction pathways and lower the activation energy for reaction (often referred to as the reaction/activation barrier) at the surface compared to the gas-phase value. The reaction rate at a given temperature is given by the Arrhenius expression:

$$k = \frac{dN}{dt} \propto e^{\frac{-E_r}{kT_s}}, \tag{2.4}$$

where $\frac{dN}{dt}$ is the number of reactants formed per second, E_r is the activation energy for the reaction in question and T_s is the surface temperature. The exponential dependence gives that even small decreases in activation energy will result in much higher reaction rates.

Catalytic surface reactions are usually classified according to their reaction mechanisms. The most commonly observed mechanism was first proposed by Langmuir and Hinshelwood and is therefore called the Langmuir-Hinshelwood (LH) mechanism. The reactants first adsorb at the surface and then react. The total reaction scheme for A and B reacting to AB can be

described as:

$$\begin{aligned} A(g) &\rightleftharpoons A(ads) \\ B(g) &\rightleftharpoons B(ads) \\ A(ads) + B(ads) &\rightleftharpoons AB(ads) \\ AB(ads) &\rightleftharpoons AB(g), \end{aligned} \tag{2.5}$$

where g stands for gas phase and ads for adsorbate. One example of an LH-reaction is the oxidation of carbon monoxide to carbon dioxide at the Pt(111) surface [23].

Another catalytic reaction mechanism was proposed by Eley and Rideal (the Eley-Rideal (ER) mechanism), in which one of the reactants is adsorbed at the surface and reacts with an atom/molecule in the gas phase. This reaction scheme is described by:

$$\begin{aligned} A(g) &\rightleftharpoons A(ads) \\ A(ads) + B(g) &\rightleftharpoons AB(ads) \\ AB(ads) &\rightleftharpoons AB(g) \end{aligned} \tag{2.6}$$

Examples of the ER-reaction are much more scarce than for the LH-reaction. However, it is believed to be the mechanism behind carbon monoxide oxidation to carbon dioxide at polycrystalline ZnO surfaces [24].

2.7 Photoinduced Processes

A major difference between thermally activated surface processes and photoactivated surface processes is the energy transfer mechanism. Thermal processes are primarily initiated by energy transfer from phonons to the vibrational states of the adsorbate, see Section 2.4. The adsorbate usually remains in the electronic ground state during the entire process. A thermal desorption process is a small deviation from an established equilibrium (or part of an equilibrium). Thus, the desorption kinetics can be derived by using thermodynamic equilibrium approaches.

The situation is quite different for photoinduced processes (unless the photons only give rise to heating), as for these cases the system is in non-equilibrium. This can make thermally inaccessible reactions possible by photon irradiation even at low temperatures. One example is the oxidation of CO on O/Ru(0001) [25]. The Ru-O bond has to be activated before the reaction can occur, but the energy barrier for this process is much higher (1.8 eV) than for CO desorption (0.83 eV), which means that the reaction

cannot be thermally driven since all CO desorbs before the Ru-O complex is activated. With energy provided by laser light, the Ru-O bond is activated by hot electrons formed at the Ru surface and CO-oxidation occurs.

Photoinduced (and also electron-induced) processes usually start with energy transfer into the electronic states of the adsorbate and the subsequent surface processes are determined by the relaxation of the electronically excited adsorbate. The first step in the energy transfer is the absorption of light. The photons can be absorbed directly by the adsorbates at the surface (adsorbate mediated processes) or by the substrate (substrate mediated processes) [26].

For surface photochemistry on metal and semiconductor surfaces, the dominating mechanism is substrate-mediated [27, 28]. When the photons are absorbed by the substrate, electron-hole pairs are created in the bulk. Since these electron-hole pairs have kinetic energies corresponding to high temperatures, they are usually referred to as hot charge carriers. A fraction of the hot charge carriers will reach the surface and the adsorbed molecules. When they reach the surface, they can either attach to or transfer their energy to the adsorbed molecules, thereby creating ions or excited molecules at the surface. Since this transfer represents a higher energy state the ions/excited molecules will eventually (the timescale is usually fs-ps) go through a neutralisation/deexcitation process to get back to the ground state. While doing this, the adsorbed molecules might gain enough energy to desorb from the surface, dissociate at the surface and/or react with each other at the surface [26].

The efficiency of substrate-mediated processes depends on both the optical absorption properties and the charge carrier transport properties of the substrate. Furthermore, it depends on the adsorbate-substrate interaction. The absorption properties determines how many of the incoming photons that are converted into hot charge carriers, while the transport properties (such as the mean free path and the probability for inelastic scattering) govern the number of charge carriers that reach the surface with enough energy to induce reactions. A third property that affects the total cross-section for the substrate-mediated processes is the life-time of the excited molecules/ions once created at the surface. The quenching of the excited states is much more efficient at metal surfaces than at surfaces of materials with a band gap. This leads to higher cross-sections for photo-induced processes at oxide and semiconductor surfaces than at metal surfaces. This is due to the larger probability of deexcitation via low energy electron-hole pairs in metals than in large bandgap materials [26].

For the adsorbate-mediated processes, the absorbed photon energy is what causes the electronic excitation [26]. The efficiency of the photon

absorption together with the lifetime of the excited states will determine the total cross-section (and the efficiency of the process) for the adsorbate-mediated photoinduced processes. Examples of adsorbate-mediated processes are the methane photodissociation and photodesorption at Pt(111) and Pd(111) [29, 30].

Two simple photoinduced processes are photodissociation and photodesorption, which commonly are described within the excitation-deexcitation models according to Menzel, Gomer, and Redhead (MGR-mechanism) [31, 32] and Antoniewicz [33]. Both models can be applied to both the adsorbate- and the substrate-mediated processes, and are shown schematically in Figure 2.9.

The essential features of the MGR mechanism are shown in Figure 2.9(a). The initial electronic excitation occurs by a Franck-Condon (FC) transition [1 in Figure 2.9(a)] from the electronic ground state (M+A) to either an antibonding excited state (M+A)*, or a repulsive ionic state (M^-+A^+). Both of these excited states have longer equilibrium bond lengths than the neutral ground state. This means that the minimum in the interaction energy occurs further away from the surface, as compared to the ground state. The adsorbate will therefore begin to move away from the surface (increase the bond length) and thereby transfer potential energy into kinetic energy [2 in Figure 2.9(a)]. This holds until the equilibrium bond length (minimum potential energy) is reached. If the adsorbate continues to move away from the surface, kinetic energy is converted into potential energy again. The amount of time that the adsorbate-substrate system spends in the excited/ionic state is determined by the lifetime of the excited/ionic state. This time is usually short enough that a second Franck-Condon transition [3 in Figure 2.9(a)] deexcites the adsorbate-substrate system down to the ground state before the minimum potential energy is reached. For the (M+A)* state, the deexcitation occurs by creation of electron-hole pairs in the substrate, whereas the ionic state is neutralised by tunnelling of electrons into (the positive ion case, A^+) or out of (the negative ion case, A^-) the adsorbate. If the gained kinetic and potential energy is larger than the barrier to desorption/reaction/dissociation ($E_{k'}$ >D), the adsorbate will desorb/react/dissociate [4 in Figure 2.9(a)]. If not, the adsorbate will dissipate the gained energy into the substrate and return to the vibrational ground state at the bottom of the adsorption well, and no photoinduced process will be experimentally detected.

The other mechanism proposed by Antoniewicz [33] is shown in Figure 2.9(b). Here, the initial FC-transition occurs to an attractive ionic state [1 in Figure 2.9(b)], resulting in the adsorbate being attracted towards the surface by its mirror image [2 in Figure 2.9(b)]. Also in this model, kinetic energy is gained in the ionic state. After a while, depending on the life-

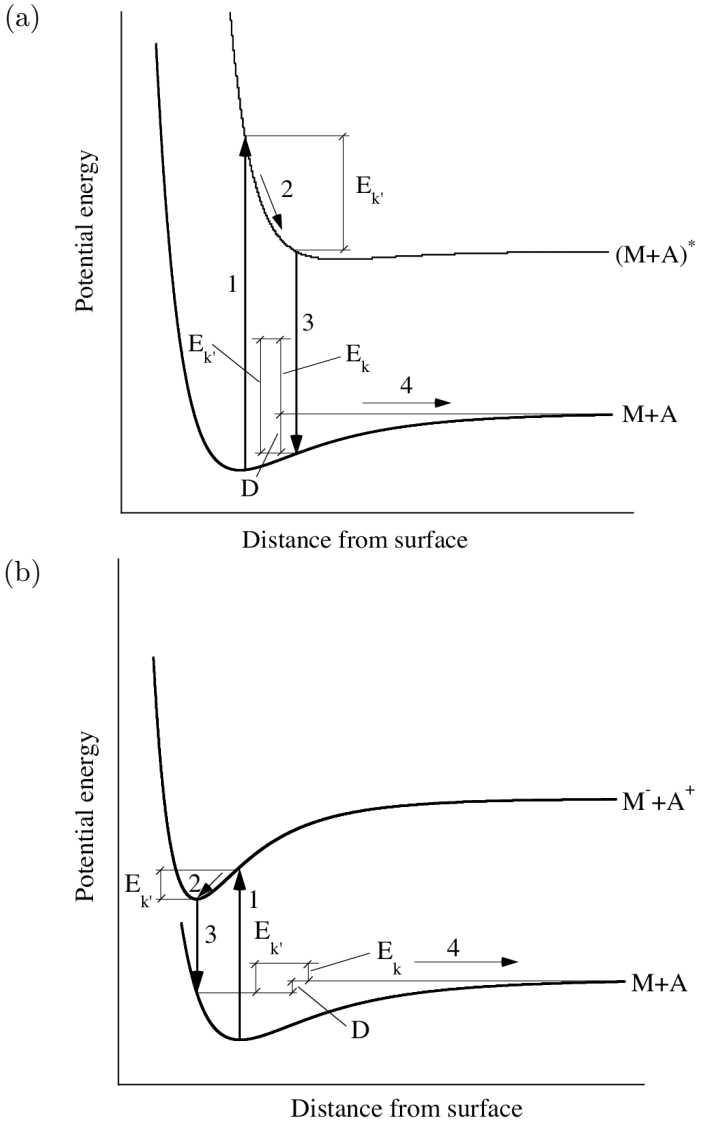

Figure 2.9: (a) Schematics of the potential energy curves involved in the Menzel-Gomer-Redhead mechanism for photodesorption adapted from [31, 32]. (b) Schematics of the potential energy curves involved in the Antoniewicz mechanism for photodesorption adapted from [33].

time of the ionic state, a second FC-transition [3 in Figure 2.9(b)] occurs by transfer of electrons into/out of the adsorbate. Also in this case, it its the amount of gained kinetic and potential energy that decides whether any surface processes occurs [4 in Figure 2.9(b), for $E_{k'}$ >D], or if the energy is just dissipated into the substrate ($E_{k'}$ <D).

Ab initio calculations have been able to reproduce desorption probabilities and velocities of photodesorbing atoms/molecules (NO/NiO [34]), as well as identify the relevant electronically excited states (CO/NiO [35]). A recent density functional theory study managed to calculate desorption rates and reproduce the power dependence of processes that require multiple electronic transitions [36]. For a more thorough discussion of the quantum dynamics of photoinduced desorption, see [37].

2.8 Film Growth

INCLUDED in Figure 2.4 are two processes that are important for film growth at surfaces; *nucleation* and *down-diffusion*, i.e. landing on already adsorbed atoms/clusters, followed by diffusion to the edge of the adsorbed cluster and adsorption on the surface. These two processes together with the surface diffusion will establish 2D- or 3D-clusters on the surface, with details depending on the evaporation rate, substrate temperature, and energy barriers for the processes in Figure 2.4. Once the maximum number of stable clusters is reached on the surface, the clusters grow. This is the case as the average distance between clusters is small enough that the diffusing single atoms will meet a cluster and attach to it before meeting another (or more) single atom(s) to form a new nucleation site. When the clusters start to coalesce, the progress of the film growth can be described as one of three different growth modes (Figure 2.10). They are [3]:

I. Frank-Van der Merwe growth mode, also known as the layer-by-layer growth mode. As the second name implies, the metal atoms that adsorb on the surface first forms a complete layer (one atom thick = 1 monolayer, ML), before the formation of the second layer starts.

II. Volmer-Weber growth mode. Here the atoms nucleate at different points on the substrate and form three-dimensional clusters. These clusters grow with increased metal deposition and it is not until the clusters are large enough to touch each other that the film formation starts. One example of this growth mode is the adsorption of silver on graphite [38].

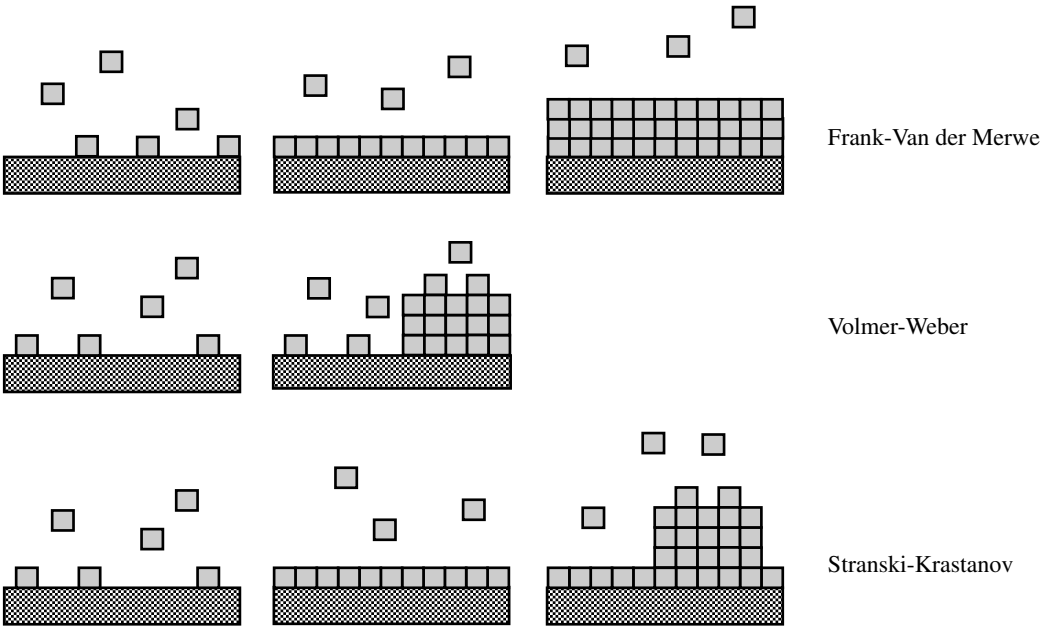

Figure 2.10: The different growth modes for metals on surfaces.

III. Stranski-Krastanov growth mode. This growth mode starts out as the Frank-Van der Merwe growth forming complete layers for the first few monolayers that adsorbs but then three-dimensional clusters begin to form on top of the layers. When the clusters begin to form, there might also be some dewetting of the initial layers from the surface. Silver on Si(100) grows in this way [39].

For metals that grow according to growth mode I and II, it is possible to alter the number of nucleation sites at the substrate by changing the deposition temperature [40], or by pretreating the substrate with etching or sputtering, thereby creating defects in the surface where the metal atoms can nucleate [38].

2.9 Sintering

The process where the mean size of particles grow over time is called *sintering* or *coarsening*. Small particles have many undercoordinated atoms (high dispersion) and are, therefore, thermodynamically unstable. The reduction of the number of undercoordinated sites is the driving force for particle sintering. Two main mechanisms are usually considered for sintering of supported particles, namely:

I. Ostwald ripening (atomic migration), where atoms or monomers are transported from smaller particles to larger ones. The transport takes place via diffusion either over the surface, or through the vapour phase. Figure 2.11(a).

II. Particle migration, where entire particles migrate over the surface and coalesce after colliding with another particle. Figure 2.11(b).

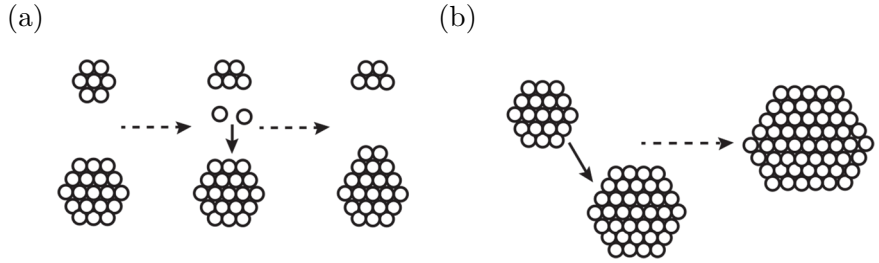

Figure 2.11: (a) Ostwald ripening (b) particle migration.

In the case of Ostwald ripening, the concentration of the diffusing species close to the edge of a nanoparticle, ρ_r is given by [41]:

$$\rho_r = \rho_\infty e^{\frac{2\gamma\Omega}{kTr}}, \tag{2.7}$$

where r is the radius of the nanoparticle, ρ_∞ the surface concentration of atomic species in equilibrium with an infinitely large particle, γ the surface energy of the particle, Ω the atomic volume, k Boltzmann's constant, and T the temperature. A small particle size (r), results in a higher concentration of atomic species close to the nanoparticle, than that for larger nanoparticles. The resulting gradient in concentration will lead to a net flux of atomic species from smaller to larger nanoparticles. Therefore, the larger nanoparticles will grow at the expense of the smaller ones. The rate-limiting step in Ostwald ripening could be either the detachment of atoms/clusters from the particle or the diffusion of these units over the surface.

Lifshitz and Slyozov [42] and Wagner [43] developed a statistical model based on Equation 2.7 that describes the ripening of spherical particles in a three-dimensional homogeneous medium. This model was later adapted for spherical caps on two-dimensional homogeneous support by Chakraverty [44]. Deviating from the statistical approach, Wynblatt and Gjostein [41] modelled instead the growth and decay of individual spherical caps on a homogeneous two-dimensional surface, determining growth rates for both detachment- and diffusion-controlled Ostwald ripening. The inclusion of the size-dependence of the surface energy of the particles by Campbell et al. has further improved the Ostwald ripening model [45, 46].

The particle migration mechanism is possible when the atomic diffusion over the surface is rapid enough that the diffusion length is comparable to the diameter of the particle [47]. If this condition is fulfilled, the random fluctuations will lead to an accumulation of adatoms on one side of the particle, making it move one atomic diameter. Over time, this will lead to Brownian motion of the entire particle on the substrate. The mean distance travelled by the particle on the substrate, X_p, is in this case given by:

$$X_p = \sqrt{4D_p t}, \tag{2.8}$$

where D_p is the particle diffusivity, and t the elapsed time. When X_p is comparable to the average interparticle spacing, particle collisions and coalescence will occur. An expression for D_p in the case of migration of a spherical bubble in a three-dimensional solid was derived by Gruber [48], whereas faceted particles were treated by Willertz and Shewmon [49]. Particle migration sintering has also been modelled by binary collisions [50, 51].

Chapter 3

Adsorbates on Graphite

In this chapter, the substrate and adsorbates that were used for Paper I-III are discussed in more detail, providing a background for the results presented in Chapter 7.

3.1 Graphite

The origin of the word graphite is the greek $\gamma\rho\alpha\phi\varepsilon\iota\nu$, meaning "to write", [52]. Graphite was first believed to be a form of lead, and referred to as "black lead". In 1779 it was shown to be a form of carbon by Carl Wilhelm Scheele [53].

Graphite consists of sheets of graphene (basal planes) stacked on top of each other. As seen in Figure 3.1, each carbon atom in a graphene sheet is bound to three other atoms within the sheet, forming the characteristic honeycomb structure. The bond is covalent in nature, formed by sp^2 hybridisation resulting in σ-and π-bands. The σ-bands are located far below (σ) and above (σ^*) the Fermi level and consequently have a rather small influence on the electronic transport properties. As carbon has four valence electrons one electron per carbon atom is delocalised. The delocalised electrons form π-bands (bonding and antibonding, π and π^*) close to the Fermi level. The bond between adjacent basal planes is van der Waals like, leading to overlapping of the π-bands. The band overlap gives graphite its semimetallic properties, owing to the partially filled conduction and valence bands [54].

The difference in bond strength within and between the graphite layers, makes it easy to break the interlayer bonds. This is one of the reasons why graphite is used in pencils; it is very easy to break the interlayer bonds and deposit graphite on a paper. For the same reason, it is an excellent (dry) lubricant in some applications. The difference in bond strength within and

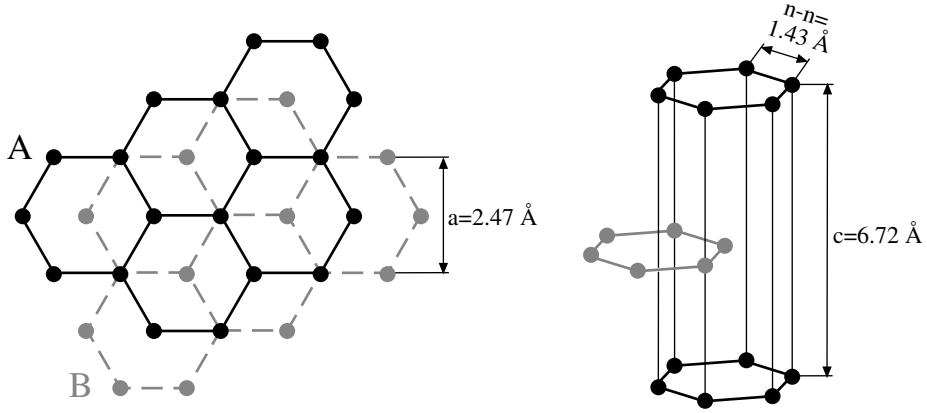

Figure 3.1: Left: Basal plane of graphite. The layers are stacked in sequence ABAB... Right: The lattice parameters and nearest neighbour distance for graphite.

between the layers gives a high in-plane conductivity (heat and electrical) together with a low conductivity perpendicular to the planes.

Owing to the saturated intralayer bonds, the graphite surface does not reconstruct upon adsorption and for the same reasons, it interacts extremely weakly with adsorbates. Notable exceptions to this weak interaction are O and O^3, which both can react with the basal plane directly, forming C-O bonds [55]. For other adsorbates, reactions with the surface mostly proceeds via defects, or the edges of the graphite basal planes.

The considerations above concern a single crystal (ideal) graphite surface/substrate. It is, however, very hard to find or make single crystals of graphite that are large enough for use in surface science studies and, thus, different kinds of synthesised graphite are generally used. One of the most common choices is the highly-ordered-pyrolytic graphite (HOPG). The first step when producing HOPG is pyrolysis of hydrocarbon gas (flowing the gas over a substrate at high temperature). This is followed by heating (up to 3600°C) under high pressure (several atmospheres) [56]. The resulting material consists of micrometersized crystallites (single crystal grains) that have a common c-axis but are azimuthally disordered. For the highest grades of the HOPG, the angle between the basal planes of the different crystallites and the c-axis is $\leq 0.1°$ and the defect density $\sim 10^9 (\mathrm{cm})^{-2}$, giving properties that are very similar to the ideal graphite case.

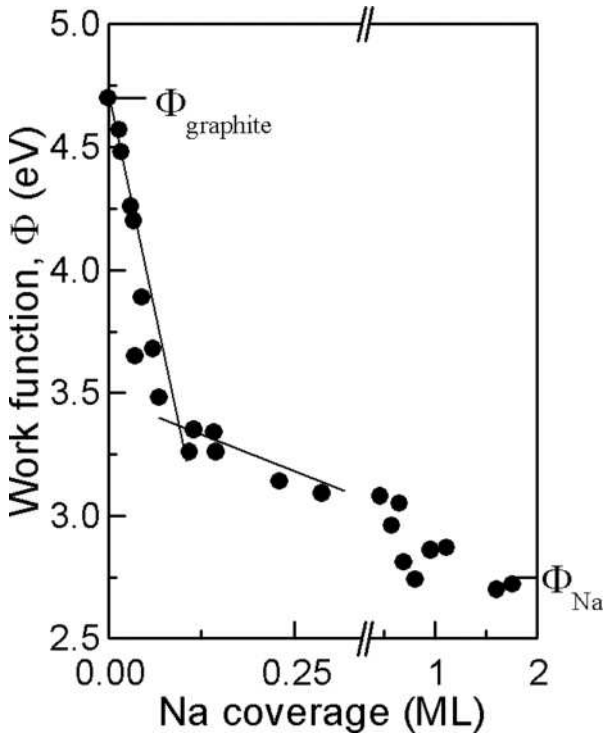

Figure 3.2: Measured work function as a function of sodium coverage (in monolayers, 1 ML=6.3x10^{14} atoms/cm^2) at the HOPG surface, from Paper I.

3.2 Sodium and Silver Deposited on Graphite

UPON adsorption of sodium (Na) on graphite, electrons are donated from the Na atoms to the graphite conduction band, resulting in a reduction of the graphite work function. The dependence of the work function on Na coverage is shown in Figure 3.2. The initial steep decrease is replaced by a slower one for coverages exceeding 0.15 ML (1 ML=6.3x10^{14} atoms/cm^2) (Paper I). The change of the slope of the work function coincides with the transition from a dispersed sodium phase (individual atoms) to cluster/island formation at the surface. Commonly denoted θ_c, values for this transition point of 0.1-0.3 ML can be found in the literature [57, 58]. The underlaying reason for the change in slope is that more charge (per atom) is transferred for the individual atoms in the dispersed phase than in the island phase. Typical experimental [57](theoretical [59]) values are around 0.2 (0.44) electrons/sodium atom for the dispersed phase and 0.04 (0.09) for the island phase. Both experimental and theoretical results point to most of the transferred charge residing within the topmost graphene layer of the substrate.

The thickness of the islands depends on the substrate temperature. For T≤90 K, monolayer island formation dominates, whereas for higher temperatures, multilayer islands form [57]. The structure of the multilayer islands has been identified as Na(110) microcrystals from scanning tunnelling microscopy measurements [60]. Ordered sodium layers, i.e. layer by layer growth, are only achieved by deposition at 40 K followed by annealing to 90 K.

Theoretical studies have shown that the preferred adsorption site for the dispersed Na phase is the hollow site [59, 61, 62], i.e. in the middle of the "honeycomb"in Figure 3.1, with adsorption energies that are close to the experimental value (Paper I) of 0.77±0.03 eV. This is lower than the cohesive energy of sodium (1.113 eV [5]) and comparison with the other alkali metals (Li, K, Rb, Cs) show that sodium has the weakest bond to graphite [59]. It has been suggested [21, 22] that the weak surface interaction (compared to sodium-sodium interaction), coupled with the relatively high ionisation potential (compared to K, Rb, and Cs) is the reason why intercalation of sodium into graphite has not been seen in adsorption studies. That lithium does intercalate already at low temperature in similar experiments, even though the ionisation potential for this element is somewhat higher, has been attributed to its smaller size and stronger surface interaction [21].

In contrast to sodium, silver (Ag) adsorption at the graphite surface does not result in noticeable changes in the work function [63]. As the workfunction of Ag is ∼4.5 eV, the work functions of silver and graphite are actually similar [64].

As mentioned briefly in Section 2.8, silver deposition on a graphite surface leads to formation of three-dimensional clusters/nanoparticles (Volmer-Weber growth mode) that increase in size with increasing deposition. The clusters/nanoparticles nucleate at defects or pits [38, 63] and have been shown to have a diameter to height ratio of ∼1.4 [38].

3.3 Water and NO Adsorption on Graphite

Water (H_2O) adsorbs molecularly on graphite at low substrate temperature (<150 K), with a coverage-independent sticking of unity [65–67]. For T≤100 K, an amorphous phase of water grows in a Stranski-Krastanov like way. Starting with 2D islands for $\theta \leq 0.5$ ML (here 1 ML=1.15x10^{15} molecules/cm^2), the growth proceeds with 3D cluster formation for θ >0.5 ML [67, 68]. This means that the number of hydrogen bonds between the molecules also increases, since the H_2O molecules in the 2D islands have a lower coordination number (number of molecules that are hydrogen-bonded to them) than the molecules in the 3D clusters. Annealing at temperatures above

130 K, or irradiation with UV light at low temperature will turn the amorphous ice at the graphite surface into crystalline ice [67, 68].

The adsorption energy has been determined to 0.45±0.03 eV/molecule (corresponding to three hydrogen bonds) [66, 67] indicating a weak interaction with the surface. Theoretical work shows water to be physisorbed at the surface with no preferred orientation at low coverages [69].

Adsorption of NO at the graphite surface at 30 K leads to the formation of NO dimers $(NO)_2$ [70]. These dimers retain their gas-phase excitation levels, since no charge exchange between the molecule and graphite occurs [71].

Chapter 4

Hydrogen Oxidation on Platinum

THIS chapter provides the background for the study of hydrogen oxidation on platinum nanoparticles in Paper IV.

4.1 Platinum

PLATINUM is an fcc noble metal that has been known to be a good catalyst for hydrogen oxidation since the 19:th century [72]. The most well-known application today is the use of platinum as catalyst in car exhaust cleaning where CO and hydrocarbons are oxidised to CO_2 and H_2O. In this and other catalyst applications, platinum nanoparticles are used. Small particles are used to maximise the surface area available for the desired reaction. As mentioned in Section 2.2, these nanoparticles exhibit preferentially (100) and (111) facets, as well as edge and corner atoms. The most stable surface facet is Pt(111), which has four different adsorption sites: on-top, bridge, fcc and hcp, see Figure 4.1.

4.2 Hydrogen on Platinum

HYDROGEN adsorbs dissociatively at platinum surfaces already at 100 K [73], with an adsorption energy of 0.80 eV [74] for the bare surface. The adsorption energy decreases when the coverage of hydrogen atoms increases, due to the repulsion between the hydrogen atoms [74]. The process has been extensively studied on single-crystal surfaces in UHV, on both Pt(111) [73, 75, 76] and stepped surfaces [77–79]. For the initial hydrogen dissociation/sticking on Pt(111) [75] and on stepped Pt surfaces that can be described

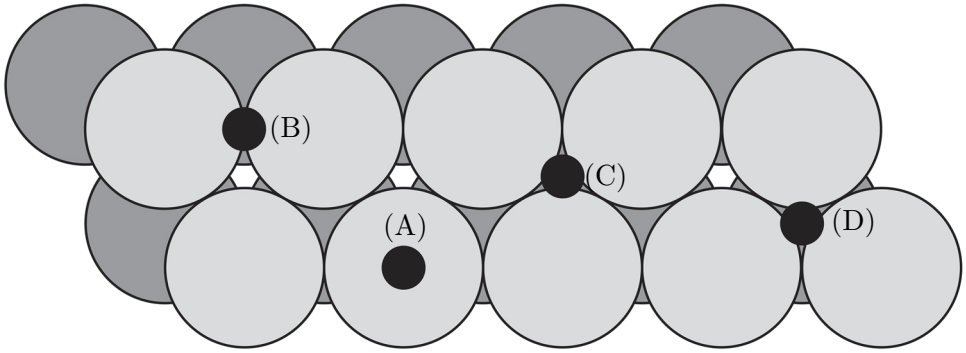

Figure 4.1: Possible adsorption sites on the Pt(111) surface. (A) on-top, (B) bridge, (C) fcc, and (D) hcp.

as a combination of Pt(111) terraces and Pt(100) steps (Pt(211), Pt(533), and Pt(755)) [78–80] three different mechanisms are believed to contribute:

I. nonactivated direct dissociation. For Pt(111) this occurs at the inner lower corner of the monatomic steps [75]. For the stepped surfaces it takes place for molecules impinging on the upper edge of a step. Mostly independent of the kinetic energy of the molecule.

II. nonactivated indirect dissociation via a molecular precursor. In the Pt(111) case, the dynamic molecular precursor traverses the surface until it either desorbs or encounters a step/defect and dissociates. The contribution to the total sticking from this process increases strongly with increasing kinetic energy of the approaching molecules [75]. In the case of stepped surfaces, molecules impinging close to the lower edge of a step diffuse to the upper edge of the step and dissociate there. The importance of this process decreases rapidly with increasing kinetic energy.

III. activated direct dissociation at Pt(111) terrace sites [75, 76]. For the stepped surfaces the contribution from this mechanism is linearly dependent on the kinetic energy of the hydrogen molecules.

Poelsema et al. [75] investigated the influence of the step sites of Pt(111) by controlled variation of the step density at the surface between 0.1%-14.1%. The mechanisms that involve step sites was found to dominate the adsorption process. This was shown by blocking the step sites with CO, which resulted in a five-fold decrease of the sticking coefficient for hydrogen on the surface [75]. Density functional theory (DFT) calculations for step-free Pt(111) show a slight preference for adsorption of atomic hydrogen at the fcc-site [81] (see

Figure 4.1). For Pt(111) with steps the preferred site is at the terrace close to the top of the step edge [75].

Groot et al. deconvoluted the contributions from the three mechanisms above for their measured data on Pt(211), Pt(533), and Pt(755), and used the dependence on kinetic energy to model the percentage of dissociation at steps as a function of nanoparticle size (assuming Wulff shape) and gas temperature [78]. For nanoparticles having a diameter of 10 nm the step contribution to the dissociation is ≈80% (≈40%) at a gas temperature of 300 K (1000 K).

4.3 Oxygen on Platinum

MOLECULAR adsorption of oxygen on different platinum surfaces has been studied extensively in the past [82–95]. On Pt(111), measurements show the adsorption to be dissociative for temperatures $\gtrsim$150 K [82]. The dissociation proceeds via a molecularly adsorbed precursor [83] and the activation energy for dissociation has experimentally been determined to be 0.29 eV [84]. The preferred binding site for the resulting oxygen atoms is the fcc hollow site [85], see Figure 4.1, and the adsorption energy has been measured to be 2.25 eV [86].

Also for stepped surfaces, the dissociation proceeds via a molecularly adsorbed precursor, on both terrace and step sites [87]. Studies of oxygen dissociation at Pt(113), Pt(211), Pt(411), Pt(335), and Pt(533) show that the steps are the preferred sites for dissociation [88–91]. The resulting oxygen atoms adsorb at the step sites [92–94]. The preferred binding site for surfaces with Pt(100) atomic steps is at the bridge site at the upper edge of the step, whereas for surfaces with Pt(111) and Pt(110) atomic steps, the preferred binding site is the fcc-hollow just behind the top edge of the step [92–94]. The adsorption energy has been measured to be 2.77 eV at the (100) atomic steps of Pt(211) and 2.32 eV at the (110) atomic steps of Pt (411) [86],[89].

The maximum O-coverage when dosing the Pt(111) surface with oxygen molecules has been measured to be 0.25 ML (1 ML Pt(111)=1.51x10^{15} cm^{-2}) [95]. It is possible to increase the coverage and oxidise the surface using atomic oxygen [96]. When Pt(111) eventually is oxidised, the majority of the formed oxide is PtO_2 (T<450 K), but PtO is also present [96]. Increasing the temperature above 500 K leads to transformation of PtO_2 into PtO, and when further heating the surface to above 600 K PtO also starts to decompose. Heating to 700 K removes all traces of the oxide [96]. For silicon dioxide supported Pt nanoparticles the oxidation process with atomic oxygen is similar; 70% of the formed oxide consists of PtO_2 and the remaining 30%

are PtO. In this case the conversion of PtO_2 to PtO starts already at 400 K, with PtO remaining stable up to 450 K. The last traces of oxide on the nanoparticles are gone at ∼800 K. It has been observed that for nanoparticles with diameters in the size range 2-6 nm, the smaller nanoparticles formed oxides more easily [96].

4.4 Hydrogen Oxidation on Platinum

THE hydrogen oxidation reaction on platinum occurs as a side reaction in a number of catalytic systems. Catalytic converters for emission control in vehicles (where the main reaction is hydrocarbon oxidation) and oxidative reforming of hydrocarbons are only two examples. Platinum catalyses this fairly simple reaction efficiently already at 130 K [97]. This should be compared to 573 K for the gas-phase reaction. The reaction is believed to take place via the following elementary steps:

I. $H_{2gas}+2^* \rightleftharpoons 2H_{ads}$

II. $O_{2gas}+2^* \rightleftharpoons 2O_{ads}$

III. $O_{ads}+H_{ads} \rightleftharpoons OH_{ads}+^*$

IV. $H_{ads}+OH_{ads} \rightleftharpoons H_2O_{ads}+^*$

V. $2OH_{ads} \rightleftharpoons O_{ads}+H_2O_{ads}$

VI. $H_2O_{ads} \rightleftharpoons H_2O_{gas}+^*$

where * denotes an empty site at the surface. Step IV and V constitute the two water formation pathways that have been observed in UHV experiments, namely sequential hydrogenation and the disproportionation reaction, respectively. The enthalpy diagram for hydrogen oxidation on Pt(111) at low surface coverage of all species is shown in Figure 4.2.

In addition to the reactions outlined above, for low (T<170 K) temperatures Scanning Tunnelling Microscopy (STM) studies have shown that the formed water reacts with the O-atoms at the Pt(111) surface to form OH-molecules [98]. These OH-molecules can subsequently form water, resulting in an autocatalytic process. This occurs at the perimeters of oxygen islands at the surface, leading to reaction fronts moving across the surface. It was suggested that this autocatalytic process is the reason why the activation energy for hydrogen oxidation is much lower (∼0.13 eV [99]) at low (<170 K) temperatures than for temperatures >300 K (0.52-0.69 eV [100, 101]). Verheij

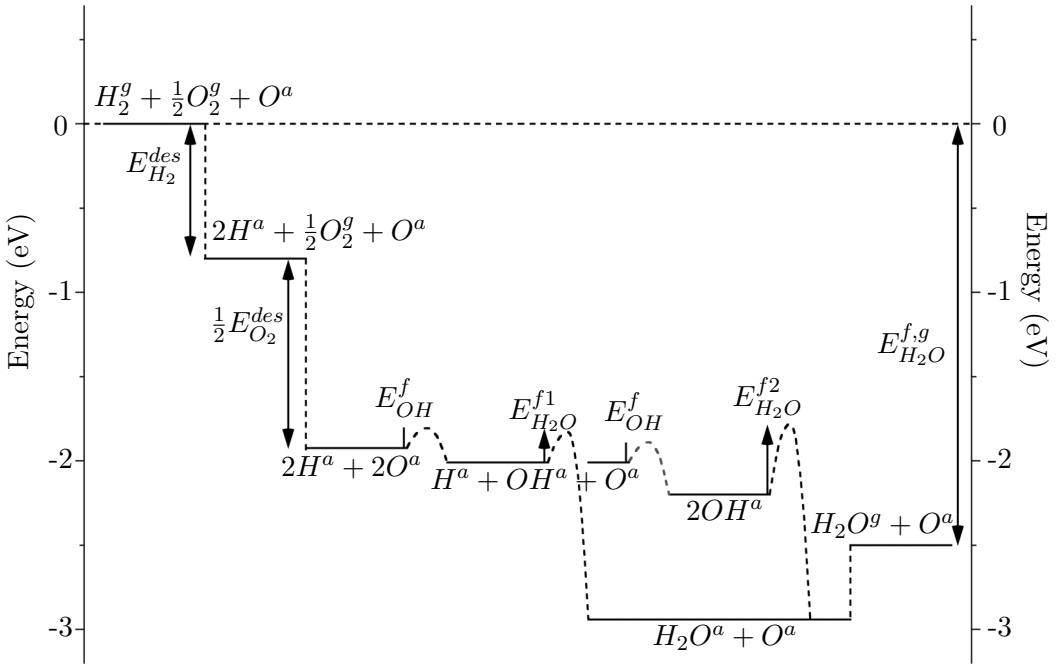

Figure 4.2: Enthalpy diagram for the hydrogen oxidation reaction on Pt(111). The energy values and their references are listed in Table 4.1

and Hugenschmidt used molecular beam relaxation spectroscopy to investigate the influence of surface defects on the hydrogen oxidation reaction on Pt(111) in the temperature interval 300-1200 K [102]. The amount of surface defects was varied by sputtering and annealing of the Pt(111) surface. The activation energy was similar for all samples but the frequency factors differed significantly, with the highest value for the surface with the highest defect density. The suggested mechanism behind this behaviour was that the reaction only takes place at certain reactive sites, and that the density of these increases with the defect density. It was suggested that oxygen diffusion will be the rate-limiting step in the case of low oxygen coverage [102].

The hydrogen oxidation reaction is exothermic as can be seen in Figure 4.2, with a reaction heat of ∼2.5 eV. Gentry et al. used this to determine activation energies of reduced and oxidised platinum wires in a gas flow via calorimetry measurements [107]. They found activation energies of 0.51±0.03 eV (0.86±0.09 eV) for the reduced (oxidised) platinum wire. Hanson and Boudart investigated the influence of nanoparticle size on the reaction rate for oxidised and reduced platinum nanoparticles [108]. They found no size-dependence for oxidised nanoparticles, whereas for the reduced particles the reaction rate constant was measured to be higher for small particles.

Quantity	Value (eV)	Reference
$E_{H_2}^{des}$	0.80	[74]
$E_{O_2}^{des}$	2.25	[86]
E_{OH}^{des}	2.0	[103]
$E_{H_2O}^{des}$	0.44	[104]
E_{OH}^{f}	0.12	[97]
$E_{H_2O}^{f1}$	0.18	[97]
$E_{H_2O}^{f2}$	0.42	[105]
$E_{H_2}^{diss}$	4.52	[106]
$E_{O_2}^{diss}$	5.16	[106]
E_{OH}^{diss}	4.45	[106]

Table 4.1: Energy values used to construct the enthalpy diagram in Figure 4.2. $E_{H_2O}^{f1}$ ($E_{H_2O}^{f2}$) is the activation energy for water formation via H_{ads}+OH_{ads} $\rightleftharpoons$ H_2O_{ads} ($2OH_{ads}$ $\rightleftharpoons$ O_{ads}+H_2O_{ads}), respectively.

Chapter 5

Optical Properties of Metallic Nanoparticles

DURING the work presented in this thesis, I have used the optical excitation in metallic nanoparticles to both induce (the photodesorption in Paper III), and probe surface processes (the indirect nanoplasmonic sensing in Paper IV and V). This chapter gives a general background to the mechanisms (optical excitation and decay) that enables probing and inducing surface processes via nanoparticle interaction with light, as well as a brief introduction to sensing using localised surface plasmon resonances.

5.1 Free Nanoparticles

THE optical response of metallic nanoparticles differs substantially from the bulk due to the confinement of the electrons within the nanosized systems. For very small nanoparticles, with discrete energy level spectra, the response will be molecule-like in the sense that it may have a non-continuous size dependence. For these clusters, it is not appropriate to use the bulk dielectric function to model the response to the incoming field. Instead electronic structure calculations could be used to calculate the electronic properties [109].

For larger systems ($10 \lesssim R \lesssim 100$ nm), which still are small compared to the wavelength of the incoming radiation if near-visible light is considered, the optical properties can be modelled with the bulk dielectric function describing the particle material, using the quasistatic approximation [110]. This approximation relies on the fact that for nanoparticles in this size range the electromagnetic field only varies with time over the system but not in space. Thus we can imagine that in each time instant a constant electric field is ap-

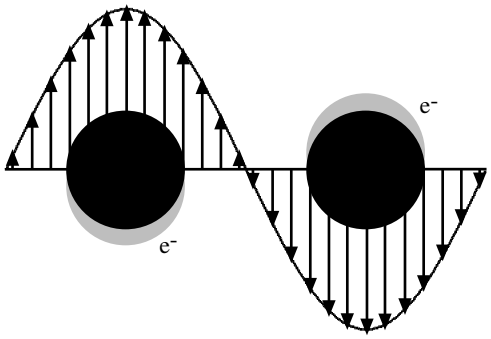

Figure 5.1: Schematic illustration of a nanoparticle plasmon. All the conduction electrons oscillate coherently in phase while the ions are stationary.

plied over the particle. Assuming that the ions are stationary and that the electrons are free to move in the nanoparticle this static field will uniformly polarise the nanoparticle. The polarisation will, in turn, give rise to an internal electric field inside the nanoparticle, which strives to depolarise it. This results in a resonance that can be rationalised as a collective excitation of the conduction electrons in the nanoparticle, a localised surface *plasmon*. Figure 5.1 is a schematic illustration of this phenomenon.

In cases where i) the imaginary part of the dielectric function of the metal, $Im(\epsilon_i) << 1$, or the frequency dependence of ϵ_i is weak and ii) the real part of the dielectric function can be approximated by the Drude model (free-electron-like metal and visible frequencies, i.e. low damping) the plasmon frequency of a spherical nanoparticle is given by [110]:

$$\omega = \frac{\omega_p}{\sqrt{1 + 2\epsilon_m}} \tag{5.1}$$

with $\omega_p = \sqrt{\frac{ne^2}{\epsilon_0 m_e}}$ being the bulk plasmon frequency, n is the volume density of free electrons, m_e is the electron mass, e is the elementary charge, and ϵ_m is the dielectric constant of the medium surrounding the nanoparticle.

The Drude model for the dielectric function only includes the response of the "free" electrons to the electromagnetic field but ignores the contribution from the more localised electrons. In the case of the noble metals that have filled d-bands, this is a large oversimplification, as excitation of electrons from the topmost d-band to the empty states in the conduction sp-band will have a large influence on the dielectric function of the material. For example, the free electron model predicts the bulk plasmon energy of silver to be ∼9.2 eV and the nanoparticle plasmon energy for a spherical silver nanoparticle to be ∼5.6 eV. The contribution from interband transitions from the 4d to the 5sp band results in a downshift of the bulk plasmon energy

in silver to ∼3.8 eV and the nanoparticle plasmon energy for a spherical silver nanoparticle is shifted to ∼3.6 eV [110]. It is, however, not only the metal itself that influences the plasmon resonance for a nanoparticle in the quasistatic regime. The shape and the size of the nanoparticle also influence the energy of the resonance(s) that occur [110]. If the nanoparticle is shaped like an ellipsoid with three different axes, the polarisability tensor will have three different resonance frequencies. For a spheroid, where two of the axes are the same, there will be two different resonance frequencies along the long and short axes, respectively. To be able to excite all resonances for non-spherical nanoparticles, the orientation of the nanoparticles relative to the electromagnetic field is important. The electromagnetic field needs to have a component along the axis that the resonance is associated with to be able to excite it. In an ensemble of free nanoparticles this condition is usually fulfilled at least for some nanoparticles, since their orientation is not fixed in space. For nanoparticles on substrates however the condition is not necessarily met.

When the size of the nanoparticle increases, the quasistatic approximation is no longer valid since the phase of the incoming electromagnetic radiation is no longer constant in space over the nanoparticle. The retardation of the field over the nanoparticle results in a size-dependence of the plasmon resonance energy. As the size of the nanoparticle increases the resonance energy of the localised nanoparticle plasmon decreases [110].

Another difference compared to the quasi-static case is that excitation of higher order multipoles becomes possible. In the quasistatic case, only excitation of dipolar modes is possible whereas for larger nanoparticles also higher order multipolar mode excitation occurs. The theory for calculating the plasmon resonance energies for spherical metal nanoparticles was developed by Mie in 1908 [111]. It was initiated by the observation that the colour of solutions containing small gold nanoparticles depended on the size of the latter. Therefore nanoparticle plasmons are often referred to as Mie plasmons.

5.2 Supported Nanoparticles

The discussion in the previous section has been limited to individual free nanoparticles in a homogeneous medium. For nanoparticles that are supported on a substrate, additional effects that influence the Mie plasmon energy come into play. The first one is that the nanoparticle surrounding is no longer homogeneous, which makes the calculation of the plasmon energy more complicated. As a first approximation of this effect, the substrate is

usually replaced by an effective medium surrounding the nanoparticle. The dielectric function of this medium is taken to be an average value of the dielectric function for vacuum and the dielectric function of the substrate, ϵ_s [110],

$$\epsilon_m \approx \frac{1}{2}(1 + \epsilon_s). \tag{5.2}$$

This estimate is then used to calculate the plasmon energy in the same way as outlined in Section 5.1. In addition to the shifts in resonance energy that the presence of the substrate induces, it also enhances the amount of multipolar mode excitation that occurs. This effect is due to the substrate being polarised by the nanoparticle plasmon excitation [112].

Not only the substrate but also the chemical environment affects the plasmon resonance energy of metallic nanoparticles. First of all, the chemisorption of molecules at the nanoparticle surface will cause changes in the electron density at the surface due to the formation of chemical bonds between adsorbate and nanoparticle, see Section 2.3. As it is the electronic structure that determines the plasmon resonance energy (through the dielectric function) this will cause shifts of the plasmon resonance energy. How large the shifts are, and in which direction along the energy axis they occur, is determined by the strength and the nature of the chemical bond. Another possible scenario is that the adsorbed molecules diffuse into the nanoparticle and thereby create a layer with different properties from the nanoparticle itself, e.g. by hydrogen diffusion into palladium nanoparticles. Two consequences follow from this. First the environment of the metallic nanoparticle changes and this will affect the nanoparticle resonance energy. Secondly, the nanoparticle size diminishes which also causes a change in the resonance energy [113]. A third scenario is that the molecules neither form a chemical bond, nor diffuse into the nanoparticle, but only physisorb at the surface. If they have a different refractive index than the effective medium this will also shift the resonance energy.

For ensembles of supported nanoparticles, the electromagnetic coupling between neighbours will also influence the energy of the plasmon. Benia et al. [114] studied the energy shift for the out-of-plane plasmon of dome-shaped nanoparticles as a function of particle density. They found a shift towards higher energy with decreasing nanoparticle-nanoparticle distances, which was attributed to destructive dipole-dipole coupling. The effect of particle spacing for particle pairs was investigated by Gunnarsson et al. [115] and they found strong shifts toward lower resonance energy with decreasing particle separation for the in-plane plasmon mode located along the nanoparticle-nanoparticle axis. The largest shifts were observed for nanoparticle spacings that were smaller than the nanoparticle diameter. Even for amorphous

arrays of nanoparticles there will be coupling between the nanoparticles. Antosiewicz et al. described the amorphous array (which only exhibits short-range order) as an average particle surrounded by a continuum of dipoles [116]. This model could successfully predict the experimentally observed oscillatory behaviour of the peak position, the extinction at peak value, and the linewidth as a function of the minimum interparticle distance (in particle diameters) in the amorphous array. The most pronounced oscillations occurred for the largest particles investigated, which is reasonable, since the scattering efficiency (and therefore the radiative coupling) increases with particle size.

After the initial excitation, the plasmon decays by transferring its energy to the environment or by dissipating it internally into heat. Available decay processes are [110]: excitation of electron-hole pairs (Landau damping), phonon excitation (heating of the nanoparticle), photon emission (radiation damping), emission of photoelectrons, thermal evaporation of atoms/molecules from the nanoparticle, and non-thermal dissociation/ desorption of nanoparticles (the effect has been observed for Na nanoparticles on LiF [117]). The most important decay mechanisms for metallic nanoparticles are Landau damping and radiative damping. For small nanoparticles, Landau damping dominates, but as the volume and amount of electrons participating in the plasmon excitation increases (increased dipole moment) radiative damping becomes more and more important [118]. However, it is not only the size but also the material of the nanoparticles that decides the decay mechanism for the plasmons. This is the case since a material that allows for interband transitions to take place in the energy range of the nanoparticle plasmons will have an additional damping mechanism, thereby suppressing radiation even for particle sizes where Landau damping is negligible. One example is plasmon decay via interband coupling in platinum and palladium nanoparticles [119].

The substrate also influences the decay of the plasmons. Nilius, Ernst and Freund [120] investigated the decay of plasmons in silver nanoparticles at strongly and weakly reduced TiO_2 surfaces. They found that at the weakly reduced surfaces, the plasmon decayed by photon emission (radiation damping). At the strongly reduced surfaces, however, the plasmons decayed by exciting electron-hole pairs in the substrate. The difference between the two surfaces is that the weakly reduced surface has a much lower charge carrier density and therefore a larger band-bending than the strongly reduced surface. The larger band-bending in the weakly reduced case results in a formation energy for electron-hole pairs in the TiO_2 that is larger than the maximum plasmon energy. This effectively 'blocks 'the electron-hole pair formation decay path and promotes the radiative plasmon decay instead.

When the nanoparticles and/or the substrate are covered by adsorbates,

the decay processes might induce surface processes/reactions. The cross-sections for substrate-mediated surface photoprocesses on the nanoparticle surface (see Section 2.7) can be substantially enhanced, since both the Landau damping and the photon emission decay paths can increase the amount of hot electrons available [118].

One example of this kind of cross-section enhancement is the study of NO photodesorption from silver nanoparticles (d=2-12 nm) on alumina that Mulugeta et al. performed [121]. They found that the photodesorption cross-section for 355 nm irradiation increased with increasing particle diameter (d) up to 5 nm, where a 43-fold increase as compared to the photodesorption cross-section of NO/Ag(111) was found. Continuing to increase the diameter resulted in diminishing cross-sections. These results were interpreted as due to saturation of the Landau damping at d=5 nm and the decrease of total plasmon oscillator strength ($\propto \frac{1}{V}$) with increasing nanoparticle size. This results in a clear maximum hot electron production at d=5 nm. The photodesorption process is driven by hot electron attachment to the NO-molecules, so as the number of hot electrons produced diminishes with increasing nanoparticle size, so does the photodesorption cross-section.

On the other hand, for adsorbate-mediated processes, the increased local field strength generated by the plasmons will be the decisive parameter. The efficiency of the surface photochemistry is determined by, for example, plasmon energy, width, decay, and lifetimes. Watanabe et al. have given a review of these effects for supported nanoparticles [118].

5.3 Localised Surface Plasmon Resonance (LSPR) Sensing

As mentioned in Section 5.2, the LSPR is sensitive to the dielectric properties of the local surroundings of the nanoparticle. Rewriting Equation 5.1 using $\omega = \frac{2\pi c}{\lambda}$ we get:

$$\lambda = \lambda_p \sqrt{1 + 2\epsilon_m} = (\epsilon_m = n^2) = \lambda_p \sqrt{1 + 2n^2}, \tag{5.3}$$

showing that the dependence of the LSPR peak wavelength on the refractive index of the surrounding medium, n, is approximately linear over a narrow range of n. Calculated values using Equation 5.3 are shown in Figure 5.2.

The change in refractive index can be measured by i) the shift in the LSPR peak wavelength, ii) the change in extinction/absorption at a fixed wavelength, or iii) the full-width-at-half-maximum [122].

This effect has been utilised to monitor biomolecular binding events, detect gases and measure pH changes to name a few examples [122]. In these

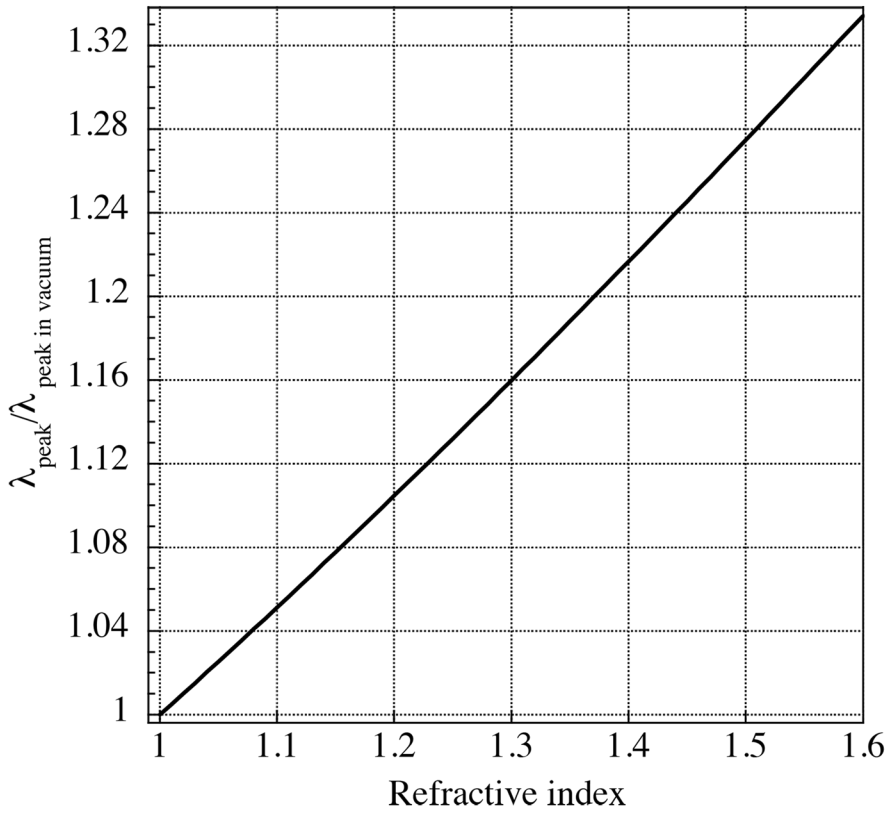

Figure 5.2: Localised surface plasmon resonance peak change with refractive index for a spherical nanoparticle. The peak wavelength is normalised to the wavelength of the resonance peak position in vacuum/air, $\lambda_{peak-in-vacuum}$.

applications, the metal (most often gold or silver) nanoparticles are covered by suitable (linking) molecules that bind strongly and specifically to the gas/bio-molecules (target molecules) to be detected. For this type of sensors, the response can be optimised by choosing a nanoparticle shape where the plasmon resonance gives rise to large field enhancements (improving the sensitivity) and as small as possible linking molecules, since the electric field decays rapidly away from the surface of the nanoparticle. This means, that the further away from the nanoparticle surface the target molecule is, the harder it will be to detect it, since the induced spectral shift of the resonance peak becomes smaller. In Section 6.7- 6.9 a detailed description of the set-up and the different types of measurements that can be made with the indirect LSPR sensing method used in Papers IV and V is presented.

Chapter 6

Experimental Set-ups and Techniques

THIS chapter presents the main measurement techniques that were used for the studies presented in the papers.

6.1 Ultra-High Vacuum (UHV) System

THE UHV-system that was used has been described in detail elsewhere [123], and here only a short description of the system will be given in order to facilitate the presentation.

An operational pressure of 2×10^{-10} torr is obtained by pumping the chamber with a turbomolecular pump in combination with a cryo pump. These pumps are backed by a mechanical pump. The system is equipped with:

- a quartz-crystal-microbalance (QCM),
- a sodium thermal evaporation source (SAES getter) and a silver thermal evaporation source,
- a doser used for water dosing and another doser that is used for dosing of gases,
- a low-energy-electron diffraction (LEED) analyser (Varian, 4-grid),
- an Auger electron spectrometer (AES, single pass, 10 kV CMA, Varian),
- an electron-energy-loss (EEL)-spectrometer (Leybold-Heraus ELS 22),

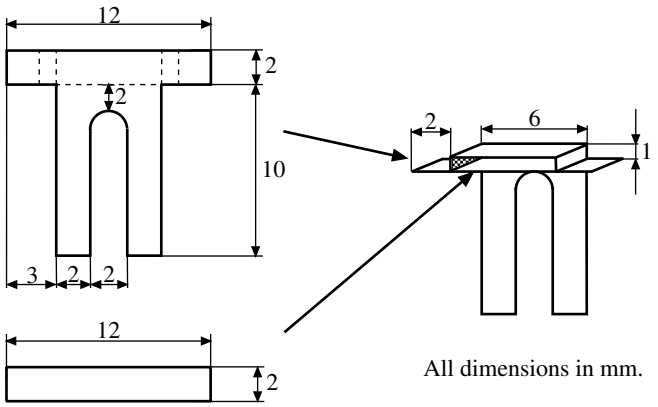

Figure 6.1: One of the two "pockets" that hold the sample. The "pocket" is formed by spot-welding the two tantalum pieces shown to the left together. The foil thickness used was 0.1 mm

- a mass-spectrometer (Balzers QMG 311), which is used for thermal-desorption-spectroscopy (TDS)-measurements and a mass-spectrometer (Balzers QMG 511) that is used for the photon-induced-desorption (PID)-measurements, and

- three windows, one of which is UV-transmitting.

The QMG 511 is mounted in an enclosure with openings for the incoming and reflected light, and the sample. This restricts the angle of irradiation of the sample to 30° with respect to the surface normal. The reflected light exits through a window, not hitting the chamber walls on the way out.

The sample holder consists of two "pockets" made out of tantalum foil, see Figure 6.1, that are spot-welded to the copper rods on the manipulator. To heat the sample a current is passed through it and cooling is provided by liquid nitrogen. The temperature range available with this set-up is 95-1350 K. The temperature is measured by a Chromel-Alumel thermocouple that was spot-welded to the tantalum sample holder.

For the purposes of the studies in Paper I-III, we made some modifications of the gasline shown in Figure 6.2 and upgraded the data acquisition system. The new acquisition system is based on Labview programs that control the mass-spectrometers and collect the data from the EELS, the temperature ramp, the pressure gauges, and the QCM monitor.

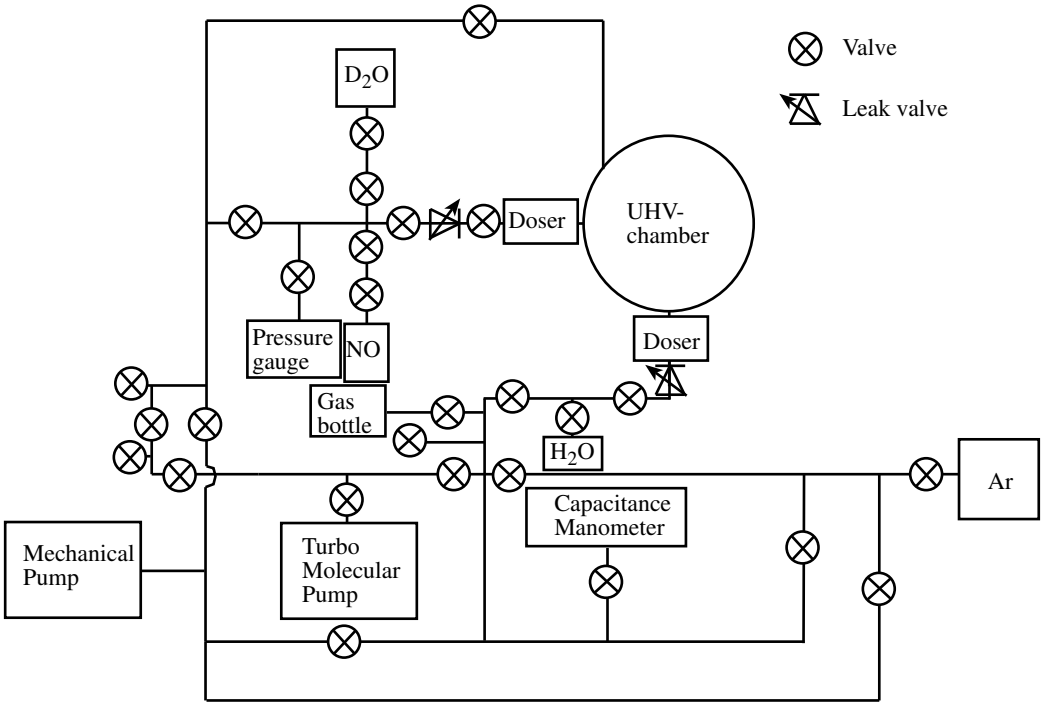

Figure 6.2: The gaslines for the HREELS UHV-system.

6.2 Preparation and Characterisation of Coadsorption Systems

The graphite sample consists of a piece of highly-ordered pyrolytic graphite (HOPG, grade ZYA Union Carbide Corp.) with dimensions 12×6×1 mm. A freshly cleaved surface was prepared by the tape method before mounting it in the chamber. Between measurements, the graphite was cleaned by annealing the sample at 1300 K for several minutes.

While the sample was cooling down it was transferred to the position for metal deposition and placed just behind the QCM. The metal source (Na or Ag depending on the experiment) was degassed and once a steady metal flux had been obtained, the QCM was withdrawn, exposing the sample to the metal flux. When the desired dose had been obtained, the QCM was inserted back in front of the sample before turning the metal source off. Thus, the QCM both measures the deposition rate of the metal and acts like a "flag"that starts/stops the deposition in a controlled way.

Next, the sample was moved into gas dosing position, where a movable doser, see Figure 6.2, was brought as close as possible, giving a sample-doser distance of ∼2 mm during dosing. This was done to minimise the

chamber contamination. Water (Millipore, 18.2 MΩcm) was dosed after it had been subjected to repeated freeze-pump-thaw cycles in order to remove gases dissolved in the water. For NO dosing, the gaslines were pumped out and then refilled with new gas to minimise contamination.

Once the entire coadsorption system had been prepared, the sample was moved into TDS-, HREELS-, or PID-position and investigated by the respective technique. All HREELS- and PID-runs were followed by TDS-measurements before the sample was annealed and the next experiment could start.

6.3 Light Sources

Two types of light sources were used in the photo-studies, arc-lamps (continuous wave) and a pulsed laser. The arc-lamps were used initially because they are easily tunable over a wide wavelength range and the maintenance is favourable compared to the laser. The advantages of the laser are the well-defined wavelength and the superior intensity.

Two types of arc-lamps were available for the photo-studies; a xenon (Xe) and a mercury (Hg) arc lamp. The Xe-lamp in combination with a low-resolution grating spectrometer gave light intensities of the order of 2-5 mW/cm^2 in the wavelength range 300-900 nm and 10 nm FWHM. To obtain higher photon fluxes, the Hg arc lamp was used in combination with narrow band-pass filters (10 nm FWHM) that were centred at the peaks in the mercury emission spectrum (254, 289, 295, 313, 336, 365, 400, 435, 545, and 575 nm). The intensities of the light was 10-100 mW/cm^2.

For the focussing on the sample, lenses and apertures were used. To vary the intensity of incident light neutral density filters were put in the optical path. This kind of filter absorbs evenly over a wide wavelength range, from the ultra-violet to the infra-red. To avoid burning of the filters (both the bandpass and the neutral density ones) a fan was used to cool them. The intensity of the lamps was measured in air by focussing the light on a thermopile power sensor (Scientech).

The laser used in the photo-studies is a Nd-YAG-laser (Powerlite 8010, Continuum). The fundamental wavelength is 1064 nm, but it is also possible to use the three first harmonics (532, 355 and 266 nm) of the laser for irradiation. The laser generates pulses with a duration between 3 and 5 ns, depending on the optical arrangement inside the laser. Apart from delivering single pulses, the system can also generate pulses with up to 10 Hz repetition rate.

The laser is connected to an optical parametric oscillator (OPO, Sunlite

Continuum) that in combination with a frequency doubler can be used to tune the output wavelength between 225-1680 nm. The input wavelength to the OPO is 355 nm (the third harmonic of the laser). After the OPO a frequency doubler (FX1, Continuum) is mounted. This enables the generation of light in the wavelength range 225-450 nm (by frequency-doubling of light from the OPO in the range 450-900 nm), thereby giving the entire set-up a wavelength range of 225-1680 nm.

Common pulse energies for the photo-experiments were 1-5 mJ/pulse. It is important to restrict the pulse energy so that transient heating of the substrate is avoided. The pulse energy was measured in air by focussing the laser beam on a laser power energy meter (3Σ). When very low pulse energies were required (μJ/pulse), several beam splitters were placed in the optical path, in combination with neutral density filters.

6.4 Electron Energy Loss Spectroscopy (EELS)

ELECTRON Energy Loss Spectroscopy is a method that can be used to measure the vibrational (High Resolution Electron Energy Loss Spectroscopy, HREELS) and electronic excitations of adsorbates and substrates. A monochromatic beam of electrons is incident on the sample studied. The reflected (or transmitted) electrons are collected and their energy distribution (sometimes also their angular distribution) measured. In the, so-called, loss spectrum, the number of electrons is plotted against their loss of energy, that is the reduction in kinetic energy compared to the incident energy. The surface sensitivity is ensured by using electron energies in the range of 1-100 eV, which have penetration depths no greater than 10 Å [124].

An example of a vibration energy loss spectrum is shown in Figure 6.3. The intense peak at zero energy is due to the elastically scattered electrons. The width of this peak (full width at half maximum, FWHM) is a measure of the energy resolution of the system. Usually, the resolution is around 5-10 meV, but resolutions below 1 meV have been obtained. The inherent linewidth of the vibrational modes for molecules adsorbed at surfaces is in the order of 0.5-1.0 meV. The background (also known as the loss continuum) in Figure 6.3 is built up by inelastically scattered electrons. The peaks that are superimposed on the background are due to resonance scattering at specific energies corresponding to excitations in the water molecule, or in the molecule-surface bond. The different excitations are schematically shown to the right in Figure 6.3. The presence of the scissoring mode shows that the

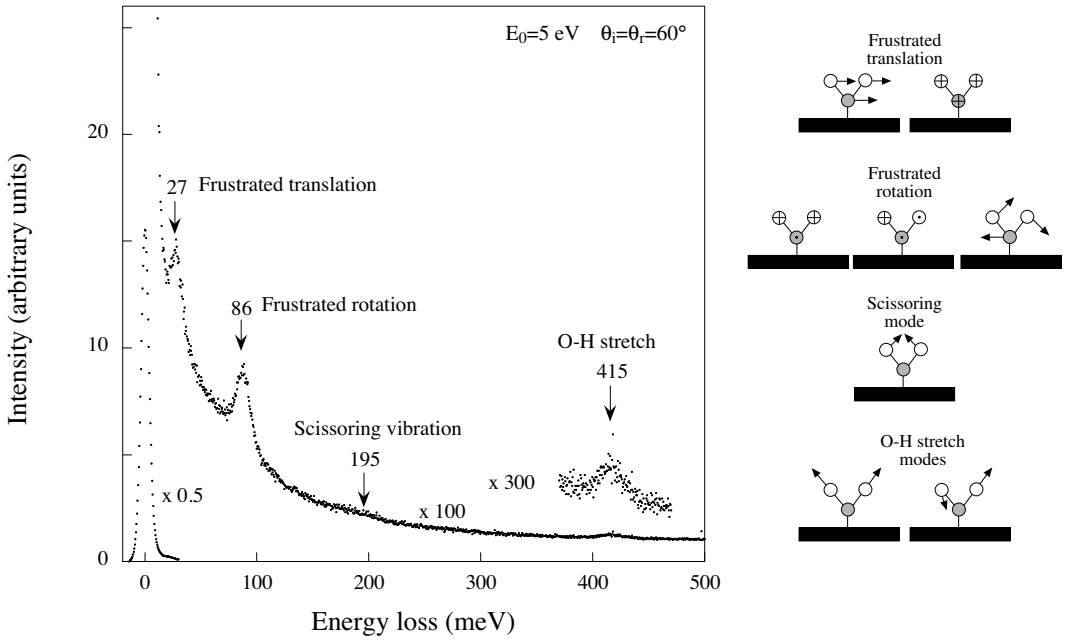

Figure 6.3: HREEL-spectrum of 0.65 ML water adsorbed on graphite (0001) at 97 K. The peaks are labelled with their vibrational modes, and the corresponding motion in the water molecule is shown to the right.

water molecules adsorb intact on graphite at this temperature. In the case of dissociative adsorption, the scissoring mode would not be present in the spectrum. The excitation mechanisms behind the energy loss for the inelastically scattered electrons are many [125]. In the solid substrate, plasmons, electron hole pairs and phonons can be excited. For adsorbates, vibrational and electronic excitations are possible. Here we are mainly interested in the vibrational excitation of adsorbates.

The two dominant scattering mechanisms are dipole scattering and impact scattering [125]. Impact scattering is the direct scattering of the electrons by the interaction with the atomic potentials of the adsorbates and the substrate. Dipole scattering is due to the dynamic electric field created by the incident electrons. This field is superimposed on the static and dynamic fields that are due to the dipole moments of the adsorbates and the electrons in the substrate. The dynamic field created by the incoming electrons transfers energy from the electrons to the substrate/adsorbates. The amount of energy that is transferred, is governed by the dielectric properties of the substrate and the absorption properties of the adsorbates, leading to resonant absorption at certain energy values. This results in peaks in the electron energy loss spectrum for energy values that correspond to the vibrational

levels of the adsorbate or specific excitations in the substrate, for example plasmon excitation. The dynamic field created by the incident electrons will be perpendicular to the surface and that is why, in dipole scattering, energy transfer can only occur in the cases where the vibrations/excitations have a dipole moment component that is perpendicular to the surface.

In impact scattering, however, this is not the case, and therefore it is sometimes possible to detect also dipole-forbidden vibrations/excitations in EELS. Another difference between the two scattering mechanisms is the angular distribution of the scattered electrons. The dipole scattered electrons are scattered in or close to the specular direction, whereas the impact scattered electrons are distributed over the entire space. This is the reason why the intensity of the EELS signal will be strongest in the specular direction and most measurements are done with the analyser in this geometry.

For HREELS, the first step in the assignment of the vibrational energy levels is to compare the frequencies found with the intramolecular vibration frequencies of the gas phase molecule. The gas phase data are obtained by infra-red-spectroscopy and values for a large number of molecules are tabulated in reference books [125]. This is not a straight forward task, since the vibration energies can shift when the molecule is adsorbed at the surface, and also since there are vibration modes between the surface and the molecule in addition to the intra-molecular vibrations found in the gas phase. A further complication arises from the presence of multiple loss peaks and the excitation of higher vibrational modes (harmonics).

The aim with the first comparison is to see if all intramolecular vibrations are still present for the adsorbed molecules (comparing the molecular "fingerprint"). If they are not, the molecule has dissociated at the surface and the vibrational frequencies measured come from the fragments. If the fragments consist of more than one atom the possible fragments can again be compared to the gas phase values for the intramolecular vibrations.

The vibrational modes can also be calculated from first principles (density functional theory). This method includes all the possible vibrational frequencies of the adsorbate, even the frustrated motion and the different frequencies due to different binding sites at the surface.

Even when it is not possible to perform a theoretical calculation of the vibrational frequencies (for large molecules), some general knowledge of the binding at the surface can be obtained. Large shifts in the intramolecular vibrations can usually be correlated to changes of the bond order. One example is the C-C vibration frequency of C_2H_2 which reduces from 250 meV in gas phase to 150 meV when adsorbed on Ni(111) [126]. The reason behind this dramatic change in vibration frequency is the reduction of the triple bond between the carbon atoms in gas phase to a single bond when

adsorbed at the Ni surface. One way to deduce this change is to compare the C-C stretching frequency with gas phase values of other large molecules that contain single carbon bonds, since for large molecules most of the constituent molecular groups retain their individual vibrational frequencies.

Last, but not least, isotope labelling can be used to pin-point the origin of the vibrational losses seen in the HREELS-spectrum, since the vibrational frequencies of the molecules/fragments depend on their mass and therefore isotope labelling will cause the peaks to shift in a manner that can be predicted.

The advantage of using HREELS compared to Infrared Reflection Absorption Spectroscopy (IRAS) is the ability of HREELS to detect also those vibrational modes of the molecule that do not have a dipole component perpendicular to the surface. In IRAS, the only available excitation mechanism for the vibrational motion of the adsorbed molecules is through dipole interaction with the incoming electromagnetic field, and hence only vibrational modes with a dipole component that is perpendicular to the surface can be excited (dipole-active modes) [127]. In HREELS, the modes that are not dipole-active can be excited by impact scattering.

Another advantage of HREELS over IRAS is that HREELS can probe vibrational energies in the range 1 meV-1 eV, whereas IRAS is restricted in the lower energy range to energies above 25 meV and in the high energy range to energies below 500 meV [127].

The sensitivity of IRAS is the same as or an order of magnitude better than for HREELS (0.01-0.001 ML for IRAS, the lower value for strong IR-absorbers [128], compared to 0.01 ML for HREELS). The resolution of IRAS is an order of magnitude better than for HREELS though (0.1 meV for IRAS compared to 1 meV for HREELS). HREELS also requires a vacuum chamber to be able to do the measurements while IRAS on the other hand can be performed at atmospheric pressure and in liquids.

The basic outline of our EEL-spectrometer is shown in Figure 6.4. The cathode emits electrons with a thermal energy distribution. These electrons are accelerated and then enter the monochromator where the electric field inside the hemisphere allows electrons of a certain energy to pass. The passing electrons are focussed onto the sample by an electrostatic lens. The reflected electrons are collected (at a certain angle, usually in the specular direction) by another electrostatic lens and enter the analyser. The analyser works in the same way as the monochromator and the energy of the electrons that are allowed to pass is varied by varying the electric field over the analyser. The passing electrons are detected by an electron multiplier and the resulting current is the signal out from the experimental set-up.

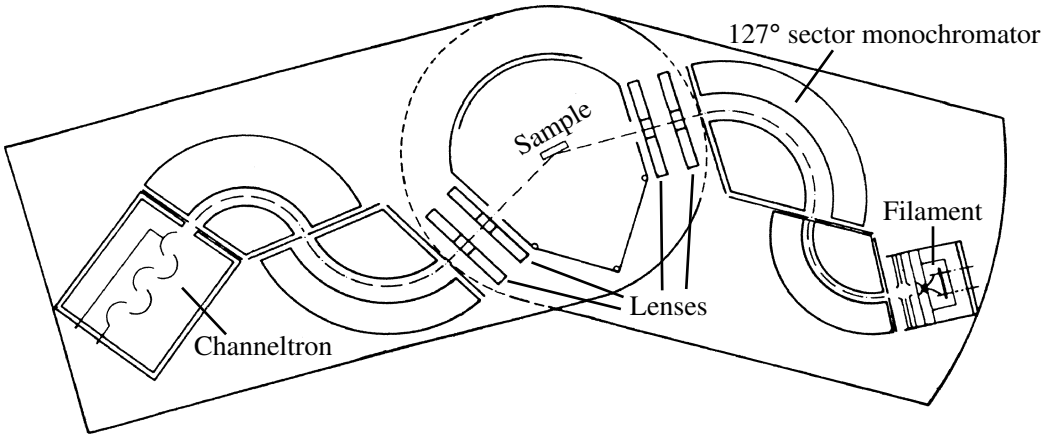

Figure 6.4: Outline of the EEL-spectrometer (ELS22).

6.5 Thermal Desorption Spectroscopy (TDS)

THERMAL desorption spectroscopy (also known as thermally programmed desorption or reaction, TPD or TPR) is used to obtain information about the energetics of the adsorbate-substrate and the adsorbate-adsorbate interactions at surfaces. Information that can be obtained in this way is the activation energies for desorption from (and sometimes also for reactions at) the surface. In addition to this information, it is also possible to determine the amount of adsorbed species at the surface (the coverage, θ) and the angular distribution of the desorbing species. One import thing to keep in mind when using TDS to obtain information about an adsorbate system, is that the method does not give information about the exact reactions on the surface or the initial state on the surface before the heating started. To obtain an assessment of the initial state at the surface or the reaction constituents, some other type of spectroscopy method is needed, for example HREELS. Thus TDS is usually used in combination with spectroscopic techniques such as X-ray Photon Spectroscopy (XPS), HREELS and structure information techniques such as Low Energy Electron Diffraction (LEED).

A typical TDS experiment is performed by controlled heating, that is temperature rise of a surface with an adsorbed overlayer and monitoring of the desorbing species during the heating. The heating rate can be linear or non-linear with time. In the early studies with this technique (in the 1960's) it was common to use fast non-linear heating rates (flash desorption). As it got easier to control the heating of the substrate linear heating rates became (and still is) the dominating technique for TDS measurements. In the studies covered by this thesis, all TDS measurements were performed with

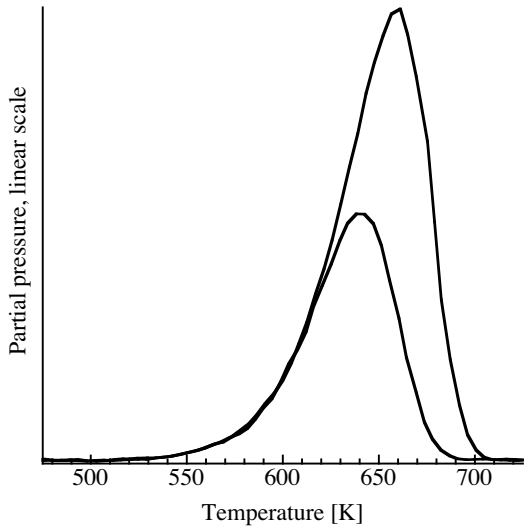

Figure 6.5: Thermal desorption of silver from a graphite (0001) surface. The desorption spectra for two different initial coverages, 3.35 and 6.38 ML Ag, are shown.

linear heating rates. Therefore a linear heating rate ($T(t) = T_0 + \beta\ t$) will be assumed in this paragraph. In our TDS-measurements, the temperature was measured by a thermo-couple that was attached to the sample and the desorbing atoms/molecules were registered by a mass-spectrometer. The signal recorded by the mass-spectrometer is proportional to the partial pressure, P_p, of the desorbing atoms/molecules. The relation between the desorption rate and the partial pressure is given by [129]:

$$\frac{dN}{dt} = \frac{V}{AkT_g}\left(\frac{dP_p}{dt} + \frac{S}{V}P_p\right), \tag{6.1}$$

where $\frac{dN}{dt}$ is the desorption rate, V is the volume of the vacuum chamber, S is the pumping speed for the vacuum chamber, A is the adsorbent area and T_g is the temperature of the gas phase. For vacuum chambers with large pumping speed-to-volume ratio and using low heating rates, $\beta = \frac{dT}{dt}$, the desorption rate will be proportional to the partial pressure (since $\frac{dP_p}{dt} \ll \frac{S}{V}P_p$). A typical thermal desorption spectrum is shown in Figure 6.5. The thermal desorption spectra show peaks in the desorption rate of the desorbing atoms/molecules. The shape and position of these peaks can give information about the activation energy for desorption and the desorption process for the atoms/molecules that are monitored. The widely used Polanyi-Wigner model assumes that the desorption rate for a species in state i on the surface can

be expressed as [129]:

$$-\frac{dN_i}{dt} = \nu_i N_i^{x_i} e^{\left(-\frac{E_i}{RT}\right)}, \tag{6.2}$$

where x_i is the desorption reaction order for state i, ν_i is the escape rate for the molecules from the surface (this is inversely proportional to the residence time for the species at the surface and usually in the order of $10^{13} - 10^{15}\text{s}^{-1}$), E_i is the activation energy for desorption and N_i is the surface coverage of molecules in state i (molecules/cm^2). An example of a first order desorption reaction is the desorption of non-interacting particles from the surface. Second order desorption reactions include associative/recombinative desorption from the surface. This can be seen by the fact that for a desorption process that requires combination of two atoms/molecules, the probability that each of theses species is available for desorption is proportional to their coverage. The total probability will, therefore, be proportional to the product of the two coverages.

For desorption reactions of zero order, the resulting desorption peak in the TPD-spectrum will be asymmetric. When the initial coverage on the surface is increased, the peak position shifts to higher temperature but the leading edge of the desorption peak remains at the same temperature. Zero order desorption is typical for adsorbates that are condensed on the substrate, so that the desorption of one adsorbate leaves the system unperturbed. Examples of zero order desorption reactions are the desorption of water and silver (see Figure 6.5) from the graphite(0001) surface.

For first order desorption reactions the desorption peak will still be asymmetric but the desorption peak temperature does not change with the change of the initial coverage on the surface [130], as long as E_i is independent of the coverage on the surface. This can be deduced from Equation 6.2 when $x_i = 1$, by finding the maximum desorption rate, which results in the relation:

$$\frac{E_i}{RT_{pi}^2} = \left(\frac{\nu_i}{\beta}\right) e^{\left(-\frac{E_i}{RT}\right)} \tag{6.3}$$

which clearly shows that the desorption peak temperature T_{pi} will not depend on the coverage as long as E_i is not coverage-dependent. An example of a first order reaction is the desorption of submonolayer coverages of silver from Si(100).

The desorption energy for a first order reaction can be estimated by the approximate relation [130]:

$$E_i = RT_{pi}\left[\ln\left(\frac{\nu_i T_{pi}}{\beta}\right) - 3.64\right]. \tag{6.4}$$

This approach does, however, require a guess of ν_i, and it also assumes that E_i and ν_i are independent of the coverage. The error when estimating the desorption energy in this way will be $\sim \pm 25\%$.

For more reliable values of the desorption energy and analysis of desorption processes that are not of the first order, lineshape analysis is used [129]. In this case, the escape rate and the desorption energy are not taken to be independent of the coverage. The first step is to evaluate $E(N)$. For a system where $\frac{dP_p}{dt} \ll \frac{S}{V}P_p$, the remaining coverage on the surface at time t after the start of the temperature ramp will be (from Equation 6.1):

$$N_t = \frac{S}{AkT_g} \int_t^\infty P dt. \tag{6.5}$$

By performing several TDS-measurements with the same rate but different initial coverages, it is possible to find a family of curves of N_t as a function of t. For a specific value of N_t, there will then be several different t-values. Each t-value corresponds to a certain temperature, T, of the adsorbent and the desorption rate, $\frac{dN}{dt}$, for this T and N_t can be determined from the corresponding desorption spectrum (using Equation 6.1). This makes it possible to construct an Arrhenius plot of $\ln \frac{dN}{dt}$ against $1/T$ for the constant coverage N_t and since the escape rate is constant at constant N_t the slope of this plot will yield $E(N_t)$. By repeating this for different N_t, $E(N)$ can be determined and plotted as a function of N. The escape rate and the reaction order is determined from the intercepts of the Arrhenius plots. The intercepts give $\ln \nu(N) + x \ln N$, so if the plot of the intercepts against $\ln N$ is linear, ν is coverage independent and the reaction order is given by the slope of the line. For coverage dependent ν, the only way to determine $\nu(N)$ is to try different integer values for x.

The discussion thus far has treated the analysis of single well-defined desorption peaks. Real measurements usually result in more complicated spectra. The spectra often consist of convolutions of consecutive peaks, giving rise to shoulders on peaks or broadening and changing of the peak shape. The origin of these peak convolutions can be the interchange from other binding states into state i during the heating, formation of different products on the surface, adsorbate-adsorbate interactions, and readsorption to the surface. Readsorption will, however, not be a substantial component as long as the pumping speed of the vacuum system is high enough. The simplest way to deal with the more complicated spectra in the analysis, is to divide the spectrum into combinations of the single-peak lineshapes and then determine the different desorption activation energies [129].

6.6 Photon Induced Desorption (PID)

PHOTON induced desorption (PID) measurements probe the interaction of light with an adsorbate/substrate system where some excitation caused by the photons induce (non-thermal) desorption/reaction of the adsorbed species. A more detailed account of the mechanisms behind photo-induced surface processes is given in Section 2.7. If the desorbing species are detected by a mass-spectrometer, the information that can be obtained is the total cross-section, σ, for the desorption process and if the initial light absorption takes place in the substrate or in the adsorbate, as well as information about the energetics of the adsorption system (same as for TDS, see Section 6.5). The term total cross-section is used, since the desorption process consists of several coupled steps where each step has its own cross-section. By combining PID with TDS or HREELS before and after the irradiation (for TDS this requires two sets of experiments, one with and one without irradiation) photo-dissociated and photo-reacted species at the surface that do not desorb during the irradiation can be detected [31].

A typical PID spectrum is shown in Figure 6.6. The partial pressure of the desorbing species is shown as a function of irradiation time. As for TDS, the desorption rate is proportional to the partial pressure as long as the pumping speed-to volume ratio of the vacuum system is high enough, see Section 6.5. The desorption rate can be described by the following rate equation:

$$\frac{d\theta_a}{dt} = -k_{des}\theta_a = -I\sigma\theta_a = -I\sigma\theta_0 e^{-tI\sigma}, \tag{6.6}$$

where I is the photon flux incident on the sample, photons/cm^{2}s, θ_a the number of molecules on the surface that are photodesorption active, molecules/cm^2, and θ_0 the initial coverage of photodesorption active molecules on the surface. To determine σ from the PID spectrum $\ln \frac{d\theta_a}{dt}$ is plotted versus t. The slope of the line yields σ, since the intensity is known. Alternatively the information from pre- and postirradiation TDS measurements can be used to determine σ. In that case σ is given by:

$$\sigma = -\frac{\ln \frac{\theta_T}{\theta_0}}{T \times I}, \tag{6.7}$$

where θ_T is the remaining coverage of the photodesorbing species after irradiating the sample for T seconds. For investigations where only the change in σ is of interest, the initial jump shown in Figure 6.6 ($= I\sigma\theta_0$) can be used as an estimate of σ, as long as the initial coverage is constant. Typical values of σ for photodesorption processes are in the range 10^{-20}-10^{-16} cm^{-2},

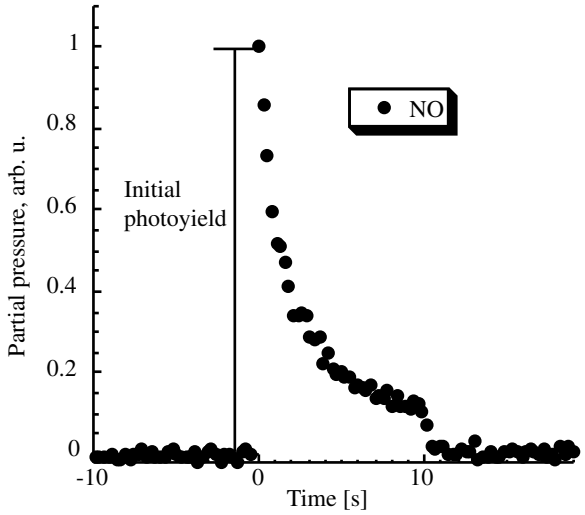

Figure 6.6: A typical PID-spectrum. The illumination started at t=0 and ended at t=10 s.

where the lower limit is set by the sensitivity of the detection equipment. For desorption processes with σ=10^{-20} and an initial coverage of 1 ML of atoms (10^{14}-10^{15} atoms/cm^2) an incident photon flux of 10^{17} photons/(cm^{2}s) will desorb 10% of the monolayer in 100 s. To get information about where the initial light absorption takes place (in the adsorbate, adsorbate-mediated process, or in the substrate, substrate-mediated process) the dependence of the cross-section on the wavelength of the incident light is measured. The wavelength dependence of the cross-section is then compared to the absorption wavelength dependence for the adsorbate and the substrate. For substrate-mediated processes the wavelength dependence of the cross-section and the substrate will exhibit the same features at the same wavelengths. If on the other hand the process is adsorbate-mediated the cross-section will follow the behaviour of the adsorbates absorption spectrum.

When pulsed lasers are used for the PID-experiments, the large energy transfer in short time might cause transient heating of the surface. This local heating dissipates too quickly to be detected in the ordinary temperature measurements, but might still cause thermal desorption of species from the surface. To distinguish between the real (non-thermal) photodesorption and the desorption caused by transient heating the dependence of the initial yield on the incident photon flux for a fixed wavelength is measured. For thermal processes, this dependence will be exponential, since thermal desorption has an exponential dependence on temperature and the temperature reached during the transient heating is proportional to the incident photon flux. In

the case of photodesorption the dependence on the incident flux is determined by the number of absorbed photons required to desorb one atom/molecule. For one-photon processes the relationship is linear, whereas for two-photon processes it is quadratic, etc.

Information about the translational energy of the desorbing molecules can be obtained by time-of-flight mass spectrometry (TOF-MS), whereas the internal energy distribution of the desorbing molecules can be probed by laser-induced fluorescence (LIF) or resonance-enhanced multiphoton ionisation (REMPI).

6.7 Flow Reactor System

THE flow reactor that was used for the studies in Paper IV and V is shown in Figure 6.7. It consists of a quartz tube (d=25 mm, L=350 mm) inside a resistive heating coil, which is insulated with glass fibre and protected by a metal cover. A thermocouple (C-Type, Omega, U.K.) positioned inside the reactor, close to the gas inlet, gives the temperature readout to the PID-regulator (Eurotherm 3508, U.S.A.) that is used to control the gas temperature. The reactor inlet is connected to a set of mass flow regulators (Bronckhorst, the Netherlands) with working ranges from 10 to 1500 ml/min. These mass flow regulators are controlled by a LabView program. For the measurements where very clean argon was needed (Paper V), two filters (one removing oxygen, the other removing moisture, both from Agilent, U.S.A.) were mounted before the inlet into the reactor.

A drawing of the sample holder is seen in Figure 6.8. The sample holder is made out of stainless steel and equipped with a thermocouple (C-Type, Omega, U.K.), which can be pressed onto the back side of the sample to measure its temperature. The sample is held in place by two screws.

The metal cover of the reactor has three viewports on each side, allowing optical transmission/extinction measurements to be carried out through the quartz tube. For the indirect nanoplasmonic sensing (INPS) measurements in Paper IV and V the light source (AvaLight-HAL, Avantes, Germany) was connected to one of these ports via an optical fibre (600 micron core, Ocean optics, USA). A collimating lens (Ocean optics, USA) was put between the fibre and the viewport. The resulting collimated light beam passed through the front of the reactor tube, the sample, and the back of the reactor tube to another viewport. This viewport was also connected to a collimating lens and an optical fibre, and through these to an array spectrometer with a fixed grating (AVA-Spec 1048, Avantes, Germany). The resulting extinction spectra were treated and analysed for LSPR peak/centroid position in real-

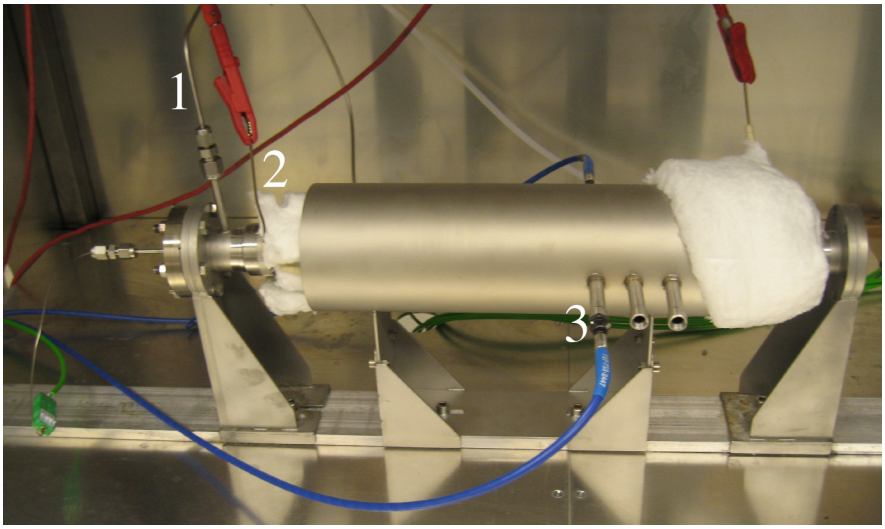

Figure 6.7: The flow reactor. 1.Gas inlet. 2. Heating coil. 3.Viewport connected to a collimating lens and an optical fibre.

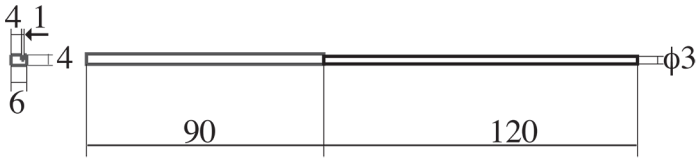

Figure 6.8: The sample holder for the reactor. All dimensions in mm.

time, using the Insplorer® software (Insplorion AB, Sweden).

6.8 Sample-Preparation and Imaging

Two types of samples were used for the reactor studies, INPS-chips and Transmission Electron Microscopy (TEM)-windows. The INPS-chips consist of borofloat glass support (15x15(mm)^2) decorated with gold nanodiscs (h=20 nm, w=80 nm) in a quasi-random arrangement. The nanodiscs are fabricated using hole-mask colloidal lithography [131]. The different steps in this process are shown in Figure 6.9. Briefly they consist of:

I. Clean borofloat glass (acetone, water, isopropanol, oxygen plasma)

II. Spin-coat PMMA on sample. Bake in 453 K for 10 min. Oxygen plasma. Charge the PMMA-layer by immersion in PDDA. Rinse. Dry.

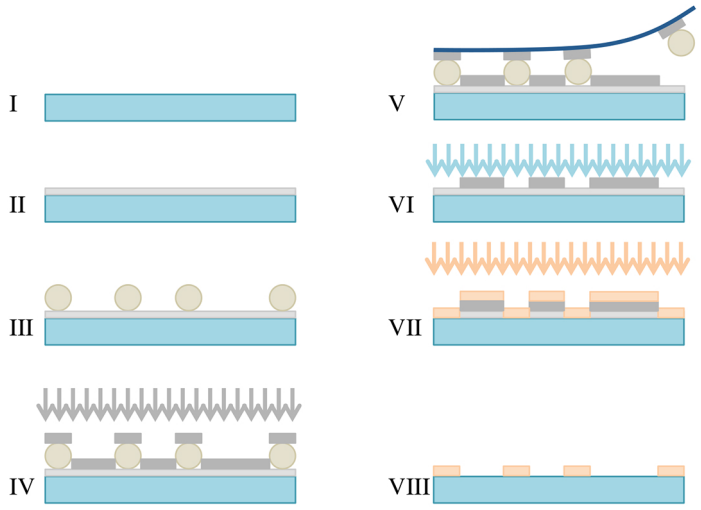

Figure 6.9: Schematic depiction of the different steps in the hole-mask colloidal lithography [131] nanofabrication method.

III. Drop solution with positively charged polystyrene particles on sample. Rinse. Blow dry.

IV. Evaporate 10 nm chromium on top of sample.

V. Tape-strip particles away.

VI. Oxygen plasma etch through the exposed PMMA. Now the deposition mask is done.

VII. Evaporate the desired height of metal (gold in my case)

VIII. Dissolve the remaining PMMA/chromium/gold structures in acetone bath, leaving only the desired nanoparticles on the surface.

After the nanodisc fabrication, the INPS-chips were heat-treated for three hours in air at 888 K, to thermally stabilise the gold nanodiscs into hexagon-shaped crystals.

A TEM-window is shown in Figure 6.10. The "window" part consists of a thin silicon nitride membrane. The TEM-windows used in the experiments were fabricated in-house using the recipe described by Grant et al. [132].

For the study in Paper IV, both the INPS-chips and the TEM-windows used were covered by 10 nm thick RF-sputtered SiO_2. The INPS-chips were then heat-treated in air at 888 K for 36 hours to stabilise the SiO_2 layer.

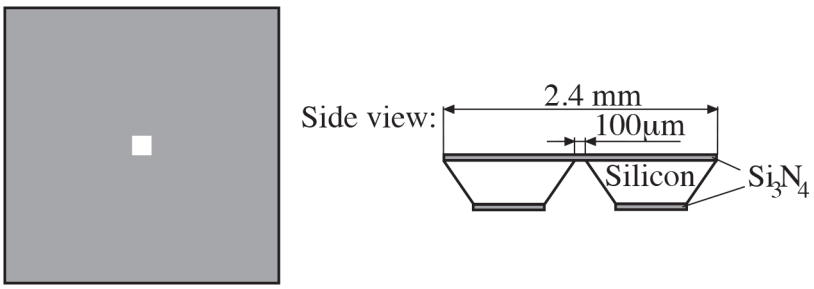

Figure 6.10: The TEM-windows used to image Pt nanoparticles (Paper IV) and clusters (Paper V).

Thereafter 5 Å Pt was e-beam evaporated onto the INPS-chips and the TEM-windows.

In Paper V, 10 nm of Si_3N_4 was plasma-enhanced-chemical-vapour-deposited on the INPS-samples. This layer was also heat-treated in air at 888 K for 36 hours, for stabilisation. The TEM-window surface already consists of Si_3N_4 (see Figure 6.10), so they were left as fabricated. Platinum clusters were in this case deposited on the samples at TUM, Germany, using a high frequency laser ablation cluster source and a transfer chamber. The cluster deposition system has been described in detail in [133, 134]. Important aspects of this deposition system are that:

- the size-selection is accomplished by sending the charged clusters through a QMS, yielding atomic-precision in the size-selection of the clusters
- the clusters are soft-landed on the surface (<2 eV/cluster), i.e. no breaking of clusters on impact, and
- since our substrates (both INPS-chips and TEM-windows) are non-conducting an electron shower was used during deposition to avoid charging of the substrates [135]

For the characterisation of the platinum nanoparticles/clusters, TEM-images were obtained at DTU, Denmark. To acquire the TEM-images of the samples with clusters (Paper V) an FEI Titan Analytical 80-300 equipped with a CEOS Cescor probe spherical aberration corrector was used, since without aberration correction it is impossible to see the tiny clusters. These TEM-images were analysed at TUM, using their in-house algorithm based on the IGOR Pro 6.22 Particle Analysis Tool (Wavemetrics, U. S. A.)[135]. The TEM-images for Paper IV were analysed using ImageJ.

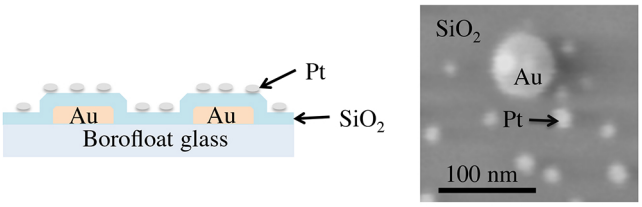

Figure 6.11: Left: Schematic depiction of the cross-section through an INPS-chip used in Paper IV. The plasmonic sensing elements here are the gold discs. Right: Scanning electron microscopy (SEM)-image [137] showing one sensing element (Au) and the smaller Pt-particles grown on the spacer layer.

6.9 Indirect Nano Plasmonic Sensing (INPS)

As the name implies, indirect nanoplasmonic sensing [136] differs from the majority of commonly used nanoplasmonic sensing techniques, see Section 5.3, in that the catalytic reaction and/or the local heat generation that is measured does not occur directly at the surface of the plasmonic sensing elements themselves. As can be seen in Figure 6.11 there is a thin dielectric spacer layer (SiO_2) separating the plasmonic sensing elements (Au) from the investigated system. The advantage of this approach is that degradation of the plasmonic sensing elements due to the reactions occurring in the system (e.g. sintering, oxidation etc.), and due to high temperatures can be minimised. Another advantage is that it makes it possible to design the size, shape and metal of the sensing element to optimise the sensitivity of the sensor, rather than having to tailor the sensing element according to the reaction that is to be studied.

I have used INPS to measure the heat released from the exothermic hydrogen oxidation reaction on platinum nanoparticles (Paper IV), and to investigate whether size-selected platinum clusters exhibit sintering or not (Paper V).

Typical extinction spectra of an INPS-sample in an argon flow at two different temperatures are shown in Figure 6.12. As the temperature increases, the extinction peak broadens and shifts to longer wavelengths. Yeshchenko et al. [138] showed that the main contribution of these changes originates from the thermal expansion of the gold particles with increasing temperature. This thermal expansion leads to a lower density, n, of free electrons in the metal particles ($n = \frac{N}{V}$, N=number of electrons, V=particle volume), and consequently to a lower plasmon frequency (longer wavelength), see Equation 5.1, in Section 5.1.

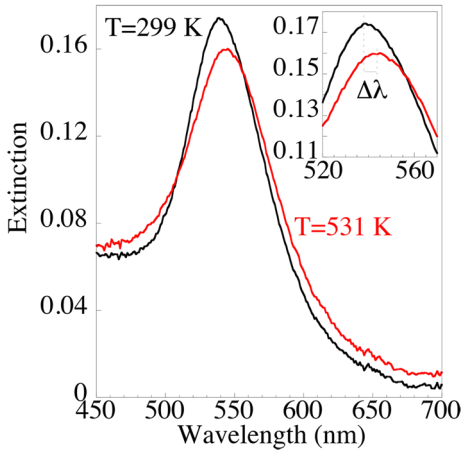

Figure 6.12: Extinction spectra of an INPS-chip in argon flow measured at two different temperatures.

Typical temperature calibration curves (linear heating of the sample in argon, no flow) are shown in Figure 6.13. They show a linear relationship between the spectral position of the LSPR peak of the extinction spectra and the sample temperature (measured by the thermocouple at the back of the INPS-chip). The three measurements depicted in Figure 6.13 also give an idea about the reproducibility of the measurements. Through this calibration, the INPS-chip can be used as a "plasmonic thermometer"that, with the current set-up, has a resolution of $\sim$1 K.

During sintering measurements, the sample temperature is kept constant to eliminate any possibility of peak shifts induced by temperature change. This way only changes in the dielectric environment of the sensing particles are recorded. These changes are induced by the rearrangement of the metal nanoparticles on top of the spacer layer during sintering, resulting in a LSPR peak position shift towards shorter wavelengths. This shift has been shown to correlate with the average size of the metal nanoparticles [139]. An example of an INPS sintering kinetics curve for platinum nanoparticles on SiO_2 is shown in Figure 6.14, together with TEM-images of the nanoparticles at the beginning and the end of the sintering experiment.

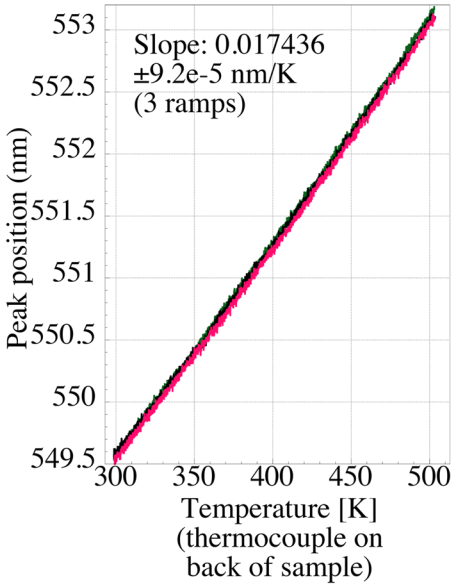

Figure 6.13: Plasmon extinction peak vs sample temperature for a temperature ramp (6 K/min) with the reactor filled with argon (no flow). Three consecutive ramps are shown to highlight the reproducibility. The sample temperature was measured by a thermocouple pressed to the back of the sample.

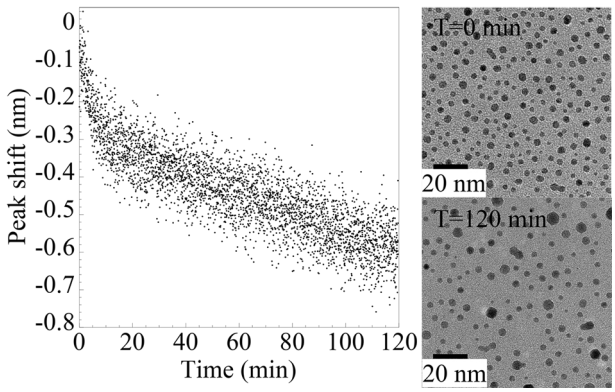

Figure 6.14: Left: INPS-signal for sintering of platinum nanoparticles in 4% O_2 in argon at 823 K. Right: TEM-images of the nanoparticles. Top: at the start of the sintering treatment. Bottom: at the end of the sintering treatment.

Chapter 7

Summary of Results

In this chapter, results are presented and discussed in terms of the phenomena presented in Chapter 2. Section 7.1 is based mainly on Paper I-II and Section 7.2 on Paper III. The results from Paper IV are presented in Section 7.3, and the results from Paper V in Section 7.4.

Throughout this chapter, the graphite mentioned in the text is highly-ordered pyrolytic graphite (HOPG). Section 7.1-7.2 concerns results from studies in UHV, whereas Section 7.3-7.4 presents results from reactor studies.

7.1 Thermally Induced Processes on Graphite

When coadsorbing water and sodium on graphite at low (95 K) temperature, the resulting surface species are determined by the amount of Na present at the surface. A critical coverage (θ_c) of 0.15 monolayers (ML) of Na was found in the study performed in Paper I. This coverage correlates with the transition from atomic sodium adsorption to cluster growth at the graphite surface, as discussed in Section 3.2. Above θ_c water adsorbs both molecularly and dissociatively, whereas for sodium coverages smaller than θ_c only molecular adsorption occurs. In both cases the adsorbates interact only weakly with the substrate, resulting in only minor amounts of carbon-containing species (for example CO and CO_2) being formed (Paper II).

For $\theta_{Na} > \theta_c$ the dissociative water adsorption leads to the formation of sodium hydroxide, most likely in the form of Na_2OH (Paper II), which forms an H-bonded network with the undissociated water molecules at the surface (Paper I). The sodium hydroxide formation is accompanied by H_2-desorption at ∼180 K. Also for $\theta_{Na} < \theta_c$ (Paper I), the coadsorbed water molecules are stabilised by the sodium present at the surface, resulting in higher desorption temperatures in the thermal desorption spectra (TDS).

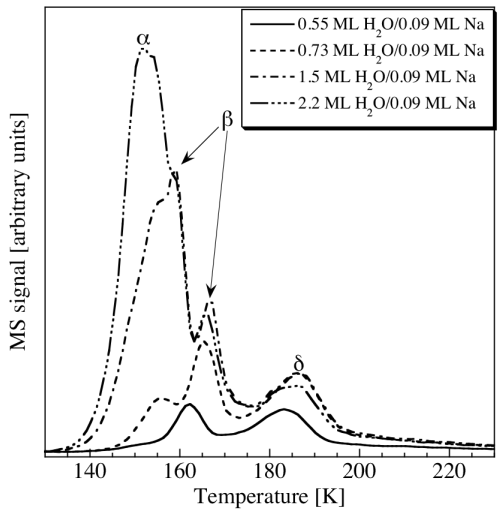

Figure 7.1: $Na+H_2O$ coadsorbed at the graphite(0001) surface.

A sequence of water desorption peaks with progressively lower desorption temperature emerges when the water dose is increased for a given sodium coverage, ending with the peak corresponding to water desorbing from a clean graphite surface (the α-peak). An example of this is given in Figure 7.1. The labelling of the peaks are in accordance with a previous study of water coadsorbed with potassium on the graphite(0001) surface [67]. The evolution of the TDS peaks, in combination with high resolution electron energy spectra (HREELS) showing an increased amount of clustered water molecules, as compared to water adsorbed on clean graphite, led to the conclusion that water-sodium complexes form at the graphite surface: a kind of hydrated ion shells. The δ-peak would then correspond to desorption from the innermost shell. By integrating the area under this peak, comparing it with known doses of water and dividing with the number of sodium atoms on the surface the number of water molecules in the innermost shell was estimated to $\sim$3.5. This is only a lower limit though, since heating the coadsorption system also results in sodium hydroxide formation. Including the hydroxide formation into the calculations results in four water molecules in the innermost solvation shell, which agrees with the theoretical value that Meng and Gao reported in [62].

The total number of water molecules stabilised to some degree by the sodium atoms was calculated by assuming that the emergence of a common leading edge in the TD spectra corresponded to the onset of desorption of unaffected water molecules (i.e. the onset of the α-peak). This yields a total of 20$\pm$3 stabilised water molecules/sodium atom.

For the Na/NO coadsorption system, the ratio of NO atoms to Na atoms will determine the chemical reactions that take place. This was established in Paper II where two distinct cases, NO:Na<1 and NO:Na>3, were found. Ratios in between resulted in a progressive change from the NO:Na<1 to the NO:Na>3-case.

Common features for all the NO:Na-ratios were that:

- all N-containing species desorbed before ∼500 K
- all C-containing species desorbed after ∼500 K
- there was coordinated desorption of Na and CO_2 at 580 and 790 K
- and CO-desorption at ∼900 K.

Taken together, these observations strongly imply that the initial reactions at the surface involve only the adsorbates forming new surface species (probably oxides) and releasing N-containing species. This is then followed by reactions between the new surface species and the graphite substrate, resulting in sodium carbonate formation. The sodium carbonates decompose in two steps (the 580 and 790 K desorption peaks) while simultaneously oxidising the graphite. The oxidised graphite causes the CO-desorption at ∼900 K.

The first critical point for the coverage ratio (NO:Na=1) occurs when all Na at the graphite surface is at least partially oxidised by NO, as evidenced by the thermal desorption spectrum no longer containing the desorption peak for unreacted sodium. Before then, no oxygen-containing nitrogen-species desorb from the surface; all nitrogen leaves the surface in the form of N_2 at 275 K. When the NO:Na ratio is increased beyond 1, nitrogen starts to leave the surface also in the form of N_2O at 410 K. The low temperature N_2-desorption peak splits into two components; the one remaining at 275 K diminishes with increasing NO-dose and the other peak shifts to higher desorption temperature (ending up at 480 K for NO:Na=3) and increases with increasing NO-dose.

The second critical point (NO:Na=3) corresponds to complete oxidation of the sodium by the adsorbed NO-molecules. This is accompanied by the presence of sodium stabilised NO at the surface, which gives rise to NO/N_2O desorption peaks at 150 K. No other new features were found in the desorption spectra.

Apart from the chemical reaction products already mentioned above for the NO/Na on graphite coadsorption system, ammonia (NH_3) desorption

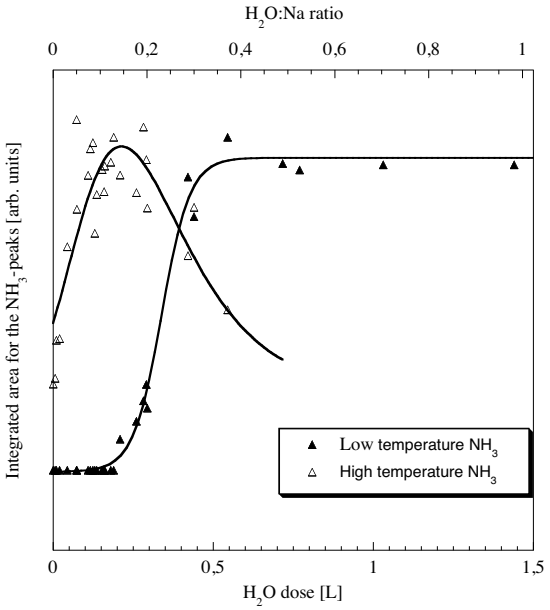

Figure 7.2: Ammonia production as a function of water dose for a fixed NO:Na ratio of 0.7 at the graphite surface. Filled triangles correspond to the low temperature ammonia peak and open triangles to the high temperature peak. The lines are only there to guide the eye.

was also seen at ∼375 K (Paper II). The source of hydrogen was determined to be water molecules adsorbed from the water pressure background in the UHV-chamber. When deliberately dosing the sample with water, the NH_3 desorption peak seen previously moved down in temperature and increased in intensity for H_2O:Na$\lesssim$0.15. Further increasing the water dose caused the desorption peak to broaden and decrease in intensity as well as the emergence of a low temperature ammonia desorption peak at 220 K. The integrated area of this low temperature ammonia desorption peak saturates at an H_2O:Na ratio of ∼0.35. The saturation value is approximately the same as the maximum value for the integrated area of the high temperature ammonia desorption peak, see Figure 7.2.

Clues to the reaction pathways for the ammonia formation are given by the overall behaviour of the coadsorption system. For high water doses, i.e. where the low temperature production of ammonia dominates, the H_2O/NO/ Na-coadsorption system starts to resemble the H_2O/Na-coadsorption system with production of sodium hydroxides and decreased CO_2-production. The decrease in CO_2-production indicates that the NO does not react with sodium hydroxides to the same extent as with unreacted Na. This conclusion is further corroborated by the fact that N_2O-desorption was seen for dosed

NO:Na-ratios<1. The reason for this is that the sodium hydroxide formation decreases the amount of Na available to the NO and therefore the effective local NO:Na ratios will be larger than 1.

In the intermediate water dose range, the simultaneous reaction of Na, NO and H_2O results in Na and CO_2 desorption at ∼615 K. Since NO does not react with sodium hydroxides and sodium hydroxides decomposing do not produce much CO_2, the origin of these desorption peaks should be the decomposition of new surface species. Possible forms for the new species are sodium formate ($NaHCO_2$) and sodium bicarbonate ($NaHCO_3$). The maximum production for the new surface species is reached for H_2O:Na∼0.15, i.e. the same ratio that results in maximum high temperature ammonia formation.

The high temperature ammonia production cannot be tied to the desorption features resulting from direct interaction between Na and NO and also not to Na and H_2O interaction, since the temperature at which the ammonia production occurs does not correlate with any of the other desorption peaks in the coadsorption system. Therefore ammonia is most likely due to the decomposition of nitrogen-containing compounds, which liberates atomic nitrogen (or amide groups) that can extract hydrogen from the system (hydroxide or hydride as it may be).

The source of hydrogen for the low temperature ammonia formation (220 K) is likely an atomic hydrogen-driven reaction that competes with the recombination (180 K) seen in the pure H_2O/Na coadsorption system. Evidence in favour of this is the dependence of low temperature ammonia production on water dose, since the amount of hydrogen made available by the sodium hydroxide production will also increase with increasing water dose up to the point when all Na is turned into sodium hydroxides, where a saturation value will be reached. Increasing the water dose after this point will not produce any more hydrogen, since there is no more unreacted sodium left at the surface, leaving the hydrogen at saturation level.

The two different reaction pathways for the two cases of ammonia production presented above also explain why the maximum ammonia production for the high temperature peak is the same as the saturation level for the low temperature ammonia. The high temperature ammonia process can extract all hydrogen present in the system, whereas the low temperature process only has access to half the hydrogen present, since the other half goes to sodium hydroxide formation. Therefore the same amount of ammonia is produced for H_2O:Na∼0.15 and H_2O:Na∼0.3.

7.2 Photodesorption of NO from Silver Nanoparticles on Graphite

THE main idea behind the photodesorption study was to investigate how the shape and size of silver nanoparticles on a surface will influence the interaction of light with that surface. This was done by monitoring the changes in cross-section for photodesorption of NO from the sample. NO was chosen as the probe molecule since its photoactivity on silver is well known [140].

The two main reasons for choosing to work with silver nanoparticles on a graphite substrate were:

- silver on graphite grows in the Volmer-Weber growth mode, resulting in well defined individual clusters, see Section 3.2.
- silver and graphite have similar work functions (4.5-4.8 eV), meaning that any changes in the photodesorption cross-sections will not be due to the lowering of work-functions with increasing silver coverage, see Section 3.2.

All the experimental details on silver nanoparticle growth, NO adsorption, thermal- and photodesorption can be found in Paper III.

Nitrogen monoxide photodesorbs from a graphite surface when illuminated with 355 nm light (Paper III). The desorption process was found to be hot charge carrier driven and substrate-mediated. In addition to the photodesorption, photodissociation of NO also takes place at the surface, resulting in formation (and desorption) of nitrogen (N_2) and nitrous oxide (N_2O) and also to some degree carbon monoxide (CO) or carbon dioxide (CO_2).

The exact relations between carbon- and nitrogen-containing desorption species could not be determined, since the mass/charge (m/e) ratios are indistinguishable for the mass-spectrometer we used for N_2 and CO (m/e$\approx$28) and N_2O and CO_2 (m/e$\approx$44). The NO photodesorption signal was however the strongest, with the cross-section being $\sim \frac{1}{6}$ of the cross-section for photodesorption of NO from Ag(111).

Adding silver nanoparticles (grown in situ to avoid oxidation) to the graphite sample, resulted in increased cross-sections for NO photodesorption. The increase compared to the bare graphite depended on the size and shape of the silver nanoparticles.

Since the number of silver nanoparticles at the surface is determined by the number of surface defects [38] the size of the nanoparticles was regulated

by the amount of silver that was deposited. The shape dependence was investigated by annealing or irradiating the clusters prior to the photodesorption experiment. Annealing at 300 K for five minutes resulted in sintering and flattening of the nanoparticles, as confirmed by EELS measurements (Paper III), whereas irradiation has been shown to cause partial evaporation of silver nanoparticles [141].

The resulting dependence of the photodesorption cross-sections on the nanoparticle size exhibited two strong local maxima. These local maxima had cross-sections approximately 20 (θ_{Ag} ≈4.5x10^{15} atoms/cm^2=θ_{Agmax}) and 14 (θ_{Ag} ≈1.5x10^{16} atoms/cm^2) times higher than the photodesorption cross-section for NO adsorbed on graphite. Annealing (300 K, 5 minutes) of the sample after silver deposition ($\theta = \theta_{Agmax}$) and prior to the dosing of NO resulted in a decrease of the photodesorption cross-section by 30-50%, whereas irradiation (≈100, 5 mJ pulses) of the sample ($\theta = \theta_{Agmax}$) before the NO exposure reduced the cross-section by 15-35%. Possible mechanisms behind the observed size and shape dependence of the cross-section for NO photodesorption from silver nanoparticle covered graphite could be:

- excitation of localised surface plasmons in the silver nanoparticles which decay by electron-hole pair creation (Landau damping), thereby increasing the number of hot charge carriers available to induce NO-photodesorption.

- electric field enhancement close to the silver nanoparticle edges, resulting in increased electron-hole pair creation at the graphite surface since that production is proportional to the field strength.

These mechanisms are illustrated in Figure 7.3.

7.3 Hydrogen Oxidation on Platinum Nanoparticles

DEPOSITING platinum on silicon dioxide results in irregular (in terms of size and shape) platinum nano-particles, due to the non-wetting of platinum on SiO_2 surfaces (Volmer-Weber growth), see Figure 7.4. Annealing this nanoparticle-film in 4% oxygen in argon induces sintering [139], and by changing the anneal time (and/or temperature) the mean size of the nanoparticles can be varied systematically. This was used in Paper IV to obtain samples where the mean size of the platinum nanoparticles was in the range 2.9≤d≤11 nm at constant total amount of Pt on the surface. In

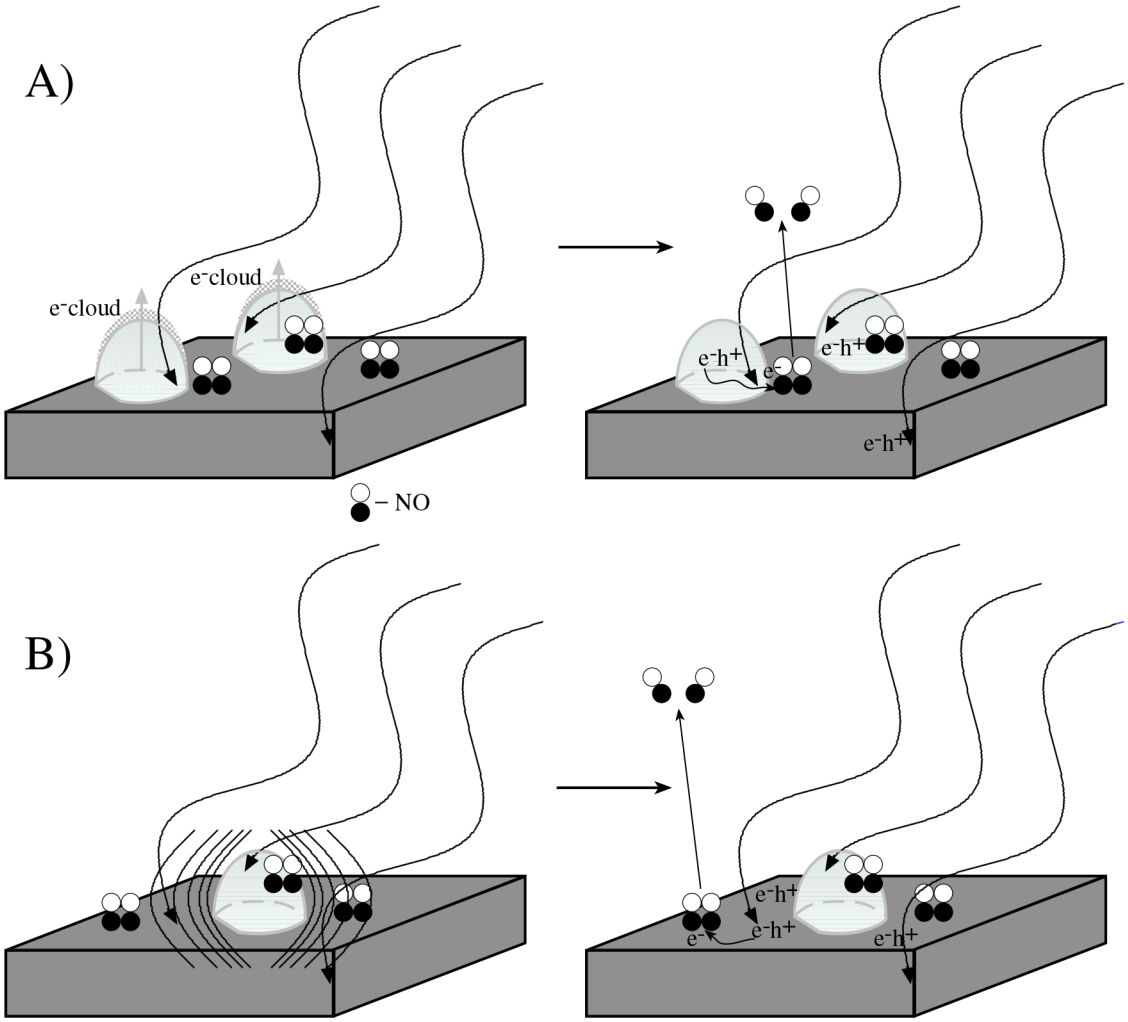

Figure 7.3: Illustration of the two mechanisms suggested in the text to explain the increased NO photodesorption when silver nanoparticles are present at the graphite surface. A) Plasmon excitation. B) Local electric field enhancement.

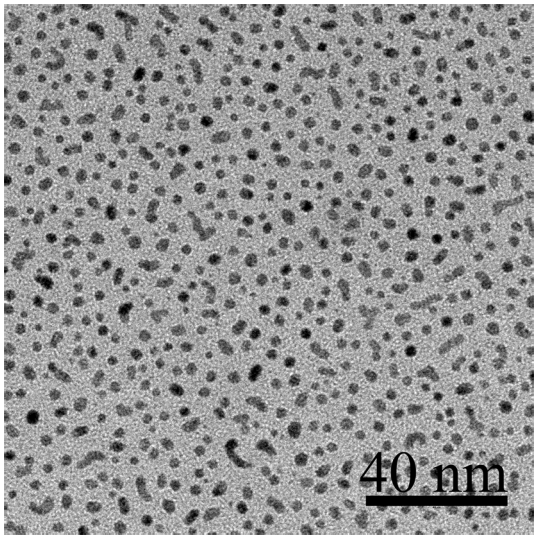

Figure 7.4: As-deposited platinum nanoparticles on silicon dioxide. Nominal film thickness 5 Å.

other words it was possible to change the dispersion while keeping the total catalyst volume constant.

After the annealing, the samples were cooled down in 4 % hydrogen in argon, to reduce the oxide formed on the nanoparticles during sintering. The reduced nanoparticles were then used as catalysts for the hydrogen oxidation reaction. Indirect nanoplasmonic sensing was used to measure the temperature of the samples during reaction, and to determine the temperature increase due to the exothermic hydrogen oxidation reaction. The apparent activation energy, E_a, for the different particles was determined via Arrhenius analysis of the temperature increase. The smallest particles (d≈3 nm) had the highest apparent activation energy (0.85 eV), and for the largest particles (d≈10 nm) the value of the apparent activation energy was ∼0.55 eV, similar to that measured on a reduced platinum wire (0.51±0.03 eV [107]).

Modelling with DFT and microkinetics showed that the increase in apparent activation energy with decreasing particle size most likely is due to the relative increase of step sites with decreasing nanoparticle size. The total reaction rate was obtained by combining the contributions from facets and steps/edges, where the fraction of step/edge atoms for each nanoparticle size was calculated by assuming Wulff-shaped particles. Using the total reaction rate to obtain E_a resulted in apparent activation energies of 0.73 eV (0.63 eV) for nanoparticles with a diameter of 3 nm (10 nm), respectively, in good agreement with the experimental values.

7.4 Sintering of Platinum Clusters

SINTERING of catalyst nanoparticles is one of the main mechanisms behind deactivation of catalysts. If the sintering mechanism is Ostwald ripening, the driving force behind the sintering should, in principle, be eliminated if all the catalyst particles have exactly the same size, i.e. same number of atoms to begin with, see Section 2.9. This hypothesis was tested in Paper V, where a cluster source with atomic precision in the size-selection of Pt clusters was used to obtain well defined samples in terms of size distribution.

Three different types of samples were used to investigate the influence of the particle size distribution on the sintering process. They were:

- only Pt_{68}-clusters, i.e. clusters with 68 atoms with a monomodal particle size distribution (PSD)
- equal amounts of Pt_{22}- and Pt_{68}-clusters, yielding a bimodal PSD
- a broad size distribution with clusters with 53 or more atoms, $Pt_{>53}$

all of the samples were prepared by softlanding the clusters on INPS-samples with a Si_3N_4 dielectric layer, or on TEM-windows (for imaging). The samples were exposed to argon at atmospheric pressure at 453 K (flow reactor) for 21 h, and the sintering was monitored by INPS, as described in Section 6.9. No sintering (shift in plasmon peak position) was detected for the sample with only Pt_{68}, whereas both the Pt_{68}+Pt_{22} and the $Pt_{>53}$ samples showed clear indications of sintering (time-dependent negative peak position shifts). This was confirmed by analysis of TEM-pictures for each of the sample types. This analysis showed clear Ostwald ripening behaviour for the bimodal size distribution; the number of Pt_{22} clusters decreased and the fraction of larger clusters around Pt_{68} increased. To eliminate particle diffusion of Pt_{22}, an additional TEM-sample with only Pt_{22} on it was treated and analysed. No sign of sintering was seen for this sample, confirming that Pt_{22}-clusters do not diffuse over the surface under the applied conditions. The reason for the sintering resistance of the samples with only one cluster size was concluded to be the efficient suppression of Ostwald ripening, by removal of its main thermodynamic driving force through size-selection.

As an additional test of the sintering resistance, the hydrogen oxidation reaction was run on a sample consisting of Pt_{68} on SiO_2 with a four times higher coverage. This resulted in very little sintering, where the driving force was provided by the small amount of double-sized clusters that were formed during cluster deposition.

Chapter 8

Concluding Remarks

The main reason behind the studies of the Na/C(0001) coadsorption systems investigated in this thesis work was to gain better understanding of the fundamental surface processes that occur in these systems. To better understand the Na/C(0001) coadsorption system, future work should include investigations of subcritical Na coverages coadsorbed with NO, as well as NO and H_2O. It would be interesting to see what happens with the water clustering observed in Paper I when NO is present at the surface. Another interesting prospect is to try to identify the different actual species at the surface, although the complexity of the system might make this hard to do.

For the photodesorption system, it was clearly shown that it is possible to maximise the photodesorption yield by choosing the right nanoparticle size range. Possible continuations of this work would be to design systems where the adsorbates adsorb preferentially on the nanoparticles or at the substrate to investigate the difference between systems where the nanoparticles are the reactive sites as opposed to "energy antennas".

The logical continuation of the hydrogen oxidation project would be to run the hydrogen oxidation reaction over size-selected platinum clusters. This would make it possible to investigate whether the apparent activation energy continues to increase with decreasing particle/cluster size. The results from Paper V indicate that the clusters should be stable over the temperature range used in the hydrogen oxidation measurements with the cluster coverage used so far. However, in order to detect the temperature increase from the reaction on the clusters, it would be necessary to either improve the temperature resolution of the INPS platform, or have a higher cluster coverage at the surface. If a higher cluster coverage is used, the first step will have to be to make sure that there is no sintering during the experiment, otherwise the INPS-signal will be hard to interpret.

As for the sintering (or rather lack thereof) of monodisperse platinum

clusters, several possible continuations exist. Use of different gases, e.g. oxygen which is a well-known promoter of sintering, higher temperatures, effects of support-cluster interaction by changing the support material, and the density of clusters are all parameters influencing the sintering that would be worth investigating.

Chapter 9

Acknowledgements

My studies have been financed by Vetenskapsrådet and the Swedish Foundation for Strategic Research.

This thesis could not have come to be without the contributions from a number of people. The following in particular:

I would like to thank my examiner and main supervisor Henrik Grönbeck for his patience and help during the writing of this thesis.

Christoph Langhammer, co-supervisor - who was always ready to discuss with, help, and encourage me. I've enjoyed working with you.

Dinko Chakarov, co-supervisor, gave me the opportunity to work with UHV- and laser equipment. I learned much from you.

Bengt Kasemo, former examiner (now retired), who introduced me to surface physics.

I owe many thanks to Michael Gleeson, who taught me a lot about laboratory work, including how much fun it can be.

Vladimir Zhdanov is gratefully acknowledged for the discussions, calculations and simulations concerning Papers IV-V.

Anders Hellman was kind enough to do density functional theory and microkinetical calculations that helped illuminate the experimental results in Paper IV.

Florian Schweinberger gave us the opportunity to work with well-defined cluster samples in a collaboration with Ueli Heiz' group at Technische Universität München.

Filippo Cavalca and Davide Deiana, both from the Center for Electron Nanoscopy at the Technical University of Denmark, took the TEM-images for the studies in Paper IV and V, respectively.

Johan B., Igor M., Dorotheé, Rebecca, Mike, Per, Jazaer, Carl H., Nina, Rafael, Gustav, Pooya, Raja, Beniamino, Anna, Viktor, and Adam all brightened my time in the office.

Håkan Ternow, Johan Bergeld, Lasse Hellberg, and Ola Löfgren have all solved computer problems for me, thank you!

Igor Zorić patiently answered all my "Kindergarten physics" questions.

All the other (past and present) members of the Chemical Physics Group are acknowledged for creating a nice working atmosphere.

Support from my family and friends is gratefully acknowledged, and a special thanks to Johan, what would I do without you?

Bibliography

[1] I. Chorkendorff and J. W. Niemantsverdriet. *Concepts of Modern Catalysis and Kinetics*. Wiley-VCH (2013).

[2] P. Christopher, H. Xin, and S. Linic. Nature Chemistry **3**, 467 (2011).

[3] A. Zangwill. *Physics at surfaces*. Cambridge University Press (1996).

[4] K. Oura, M. Katayama, A. Zotov, V. Lifshits, and A. Saranin. *Surface Science: An Introduction*. Springer Berlin Heidelberg, Berlin, Heidelberg (2003).

[5] C. Kittel. *Introduction to solid state physics*. John Wiley & Sons, Inc. (1996).

[6] H. N. Waltenburg and J. T. Yates Jr. Chemical Reviews **95**, 1589 (1995).

[7] M. Rønning, E. Bergene, A. Borg, S. Ausen, and A. Holmen. Surface Science **477**, 191 (2001).

[8] G. Wulff. Zeitschrift für Kristallographie **34**, 449 (1901).

[9] E. Roduner. Chemical Society Reviews **35**, 583 (2006).

[10] C. Henry. In U. Heiz and U. Landman (editors), *Nanocatalysis*, Nanoscience and Technology, 245–268. Springer Berlin Heidelberg (2007).

[11] The picture was made by Anders Hellman.

[12] L. Vitos, A. Ruban, H. Skriver, and J. Kollár. Surface Science **411**, 186 (1998).

[13] W. Vogel, J. Bradley, O. Vollmer, and I. Abraham. The Journal of Physical Chemistry B **102**, 10853 (1998).

[14] R. Fournier. The Journal of Chemical Physics **115**, 2165 (2001).

[15] K. Jug, B. Zimmermann, P. Calaminici, and A. M. Köster. The Journal of Chemical Physics **116**, 4497 (2002).

[16] S. A. Serapian, M. J. Bearpark, and F. Bresme. Nanoscale **5**, 6445 (2013).

[17] C. L. Jackson and G. B. McKenna. The Journal of Chemical Physics **93**, 9002 (1990).

[18] C. Nordling and J. Österman. *Physics Handbook: Elementary Constants and Unit Tables, Formulae and Diagrams and Mathematical Formulae*. Studentlitteratur, Lund Sweden (1996).

[19] Z. Jian, K. Kuribayashi, and W. Jie. Materials Transactions **43**, 721 (2002).

[20] G. Ayrault and G. Ehrlich. The Journal of Chemical Physics **60**, 281 (1974).

[21] M. Johnson, H. Starnberg, and H. Hughes. Surface Science **178**, 290 (1986).

[22] M. Caragiu and S. Finberg. Journal of Physics: Condensed Matter **17**, R995 (2005).

[23] C. T. Campbell, G. Ertl, H. Kuipers, and J. Segner. The Journal of Chemical Physics **73**, 5862 (1980).

[24] H. Chon and C. D. Prater. Discussions of the Faraday Society **41**, 380 (1966).

[25] M. Bonn, S. Funk, C. Hess, D. N. Denzler, C. Stampfl, M. Scheffler, M. Wolf, and G. Ertl. Science **285**, 1042 (1999).

[26] F. M. Zimmermann and W. Ho. Surface Science Reports **22**, 127 (1995).

[27] S. A. Buntin, L. J. Richter, D. S. King, and R. R. Cavanagh. The Journal of Chemical Physics **91**, 6429 (1989).

[28] E. Hasselbrink, S. Jakubith, S. Nettesheim, M. Wolf, A. Cassuto, and G. Ertl. The Journal of Chemical Physics **92**, 3154 (1990).

[29] K. Watanabe, K. Sawabe, and Y. Matsumoto. Physical Review Letters **76**, 1751 (1996).

[30] K. Watanabe and Y. Matsumoto. Surface Science **390**, 250 (1997).

[31] X.-L. Zhou, X.-Y. Zhu, and J. M. White. Surface Science Reports **13**, 76 (1991).

[32] P. Feulner and D. Menzel. *Laser Spectroscopy and Photochemistry on Metal Surfaces*, chapter Electronically Stimulated desorption of Neutrals and Ions from Adsorbed and Condensed Adlayers. World Scientific (1995).

[33] P. R. Antoniewicz. Physical Review B **21**, 3811 (1980).

[34] C. P. Koch, T. Klüner, and H.-J. Freund. Physical Review Letters **90**, 117601 (2003).

[35] I. Mehdaoui and T. Klüner. Physical Review Letters **98**, 037601 (2007).

[36] T. Olsen, J. Gavnholt, and J. Schiøtz. Physical Review B **79**, 035403 (2009).

[37] P. Saalfrank, M. Nest, I. Andrianov, T. Klamroth, D. Kröner, and S. Beyvers. Journal of Physics: Condensed Matter **18**, S1425 (2006).

[38] H. Hövel, T. Becker, A. Bettac, B. Reihl, M. Tschudy, and E. J. Williams. Journal of Applied Physics **81**, 154 (1997).

[39] A. Brodde, D. Badt, S. Tosch, and H. Neddermeyer. Journal of Vacuum Science and Technology A **8**, 251 (1990).

[40] M. Hanbücken, M. Futamoto, and J. A. Venables. Surface Science **147**, 433 (1984).

[41] P. Wynblatt and N. A. Gjostein. Acta Metallurgica **24**, 1165 (1976).

[42] I. M. Lifshitz and V. V. Slyozov. Journal of Physics and Chemistry of Solids **19**, 35 (1961).

[43] C. Wagner. Zeitschrift für Elektrochemie, Berichte der Bunsengesellschaft für Physikalische Chemie **65**, 581 (1961).

[44] B. K. Chakraverty. Journal of Physics and Chemistry of Solids **28**, 2401 (1967).

[45] C. Campbell, S. C. Parker, and D. E. Starr. Science **298**, 811 (2002).

[46] S. Parker and C. Campbell. Physical Review B **75**, 1 (2007).

[47] P. Wynblatt and N. A. Gjostein. Progress in Solid State Chemistry **9** (1975).

[48] E. E. Gruber. Journal of Applied Physics **38**, 243 (1967).

[49] L. E. Willertz and P. G. Shewmon. Metallurgical Transactions **1**, 2217 (1970).

[50] B. Pulvermacher and E. Ruckenstein. Journal of Catalysis **19**, 224 (1973).

[51] E. Ruckenstein and B. Pulvermacher. American Institute of Chemical Engineers Journal **19**, 356 (1973).

[52] *Oxford English Dictionary*, chapter graphite. Oxford University Press (2010).

[53] *Encyclopædia Britannica*, chapter pencil. Retrieved June 4, 2010, from Encyclopœdia Britannica Online (2010).

[54] G. D. M. S. Dresselhaus and R. Saito. *Graphite and Precursors*, chapter Electronic Band Structure of Graphites. Gordon and Breach Science Publishers (2001).

[55] H. P. Boehm. *Graphite and Precursors*, chapter Carbon Surface Chemistry. Gordon and Breach Science Publishers (2001).

[56] M. Inagaki. *New Carbons-Control of Structure and Functions*, chapter Highly Oriented Graphites. Elsevier (2000).

[57] M. Breitholtz, T. Kihlgren, S.-A. Lindgren, and L. Walldén. Physical Review B **67**, 235416 (2003).

[58] M. Pivetta, F. Patthey, I. Barke, H. Hövel, B. Delley, and W.-D. Schneider. Physical Review B **71**, 165430 (2005).

[59] K. Rytkönen, J. Akola, and M. Manninen. Physical Review B **75**, 075401 (2007).

[60] M. Breitholtz, T. Kihlgren, S.-A. Lindgren, H. Olin, E. Wahlström, and L. Walldén. Physical Review B **64**, 73301 (2001).

[61] K. Rytkönen, J. Akola, and M. Manninen. Physical Review B **69**, 205404 (2004).

[62] S. Meng and S. Gao. The Journal of Chemical Physics **125**, 014708 (2006).

[63] J. Lehmann, M. Merschdorff, W. Pfeiffer, A. Thon, S. Voll, and G. Gerber. Physical Review Letters **85**, 2921 (2000).

[64] H. Kawano. Progress in Surface Science **83**, 1 (2008).

[65] R. B. Phelps, L. L. Kesmodel, and R. J. Kelley. Surface Science **340**, 134 (1995).

[66] D. V. Chakarov, L. Österlund, and B. Kasemo. Vacuum **46**, 1109 (1995).

[67] D. V. Chakarov, L. Österlund, and B. Kasemo. Langmuir **11**, 1201 (1995).

[68] D. V. Chakarov and B. Kasemo. Physical Review Letters **81**, 5181 (1998).

[69] P. C. Sanfelix, S. Holloway, K. W. Kolasinski, and G. R. Darling. Surface Science **532-535**, 166 (2003).

[70] I. S. Nandhakumar, Z. Y. Li, R. E. Palmer, and R. Amos. Surface Science **329**, 184 (1995).

[71] W. Dianis and J. E. Lester. Surface Science **43**, 602 (1974).

[72] A. J. B. Robertson. Platinum Metals Review **19**, 64 (1975).

[73] A. C. Lunz, J. K. Brown, and M. D. Williams. The Journal of Chemical Physics **93**, 5240 (1990).

[74] B. Poelsema, K. Lenz, and G. Comsa. Journal of Physics: Condensed Matter **22**, 304006 (2010).

[75] B. Poelsema, K. Lenz, and G. Comsa. The Journal of Chemical Physics **134**, 074703 (2011).

[76] P. Nieto, E. Pijper, D. Barredo, G. Laurent, R. A. Olsen, E.-J. Baerends, G.-J. Kroes, and D. Farías. Science **312**, 86 (2006).

[77] M. J. T. C. van der Niet, A. den Dunnen, L. B. F. Juurlink, and M. T. M. Koper. The Journal of Chemical Physics **132**, 174705 (2010).

[78] I. M. N. Groot, A. W. Kleyn, and L. B. F. Juurlink. Angewandte Chemie International Edition **50**, 5174 (2011).

[79] I. M. N. Groot, A. W. Kleyn, and L. B. F. Juurlink. The Journal of Physical Chemistry C **117**, 92669274 (2013).

[80] D. A. McCormack, R. A. Olsen, and E. J. Baerends. The Journal of Chemical Physics **122**, 194708 (2005).

[81] M. J. Kolb, F. Calle-Vallejo, L. B. F. Juurlink, and M. T. M. Koper. The Journal of Chemical Physics **140**, 134708 (2014).

[82] J. L. Gland, B. A. Sexton, and G. B. Fisher. Surface Science **95**, 587 (1980).

[83] C. T. Rettner and C. B. Mullins. The Journal of Chemical Physics **94**, 1626 (1991).

[84] P. D. Nolan, B. R. Lutz, P. L. Tanaka, J. E. Davis, and C. B. Mullins. The Journal of Chemical Physics **111**, 3696 (1999).

[85] K. Mortensen, C. Klink, F. Jensen, F. Besenbacher, and I. Stensgaard. Surface Science **220**, L701 (1989).

[86] E. Karp, C. Campbell, F. Studt, F. Abild-Pedersen, and J. Nørskov. The Journal of Physical Chemistry C **116**, 25772 (2012).

[87] A. T. Gee and B. E. Hayden. The Journal of Chemical Physics **113**, 10333 (2000).

[88] T. Yamanaka, T. Matsushima, S. ichiro Tanaka, and M. Kamada. Surface Science **349**, 119 (1996).

[89] V. Fiorin, D. Borthwick, and D. A. King. Surface Science **603**, 1360 (2009).

[90] A. Rar and T. Matsushima. Surface Science **318**, 89 (1994).

[91] H. Wang, R. Tobin, D. K. Lambert, C. L. DiMaggio, and G. B. Fisher. Surface Science **372**, 267 (1997).

[92] Ž. Šljivančanin and B. Hammer. Surface Science **515**, 235 (2002).

[93] P. J. Feibelman, S. Esch, and T. Michely. Physical Review Letters **77**, 2257 (1996).

[94] P. Gambardella, Ž. Šljivančanin, B. Hammer, M. Blanc, K. Kuhnke, and K. Kern. Physical Review Letters **87**, 056103 (2001).

[95] J. L. Gland. Surface Science **93**, 487 (1980).

[96] L. K. Ono, J. R. Croy, H. Heinrich, and B. R. Cuenya. The Journal of Physical Chemistry C **115**, 16856 (2011).

[97] T. A. Germer and W. Ho. Chemical Physics Letters **163**, 449 (1989).

[98] S. Völkening, K. Bedürftig, K. Jacobi, J. Wintterlin, and G. Ertl. Physical Review Letters **83**, 2672 (1999).

[99] K. Ogle and J. White. Surface Science **139**, 43 (1984).

[100] J. N. Smith Jr. and R. L. Palmer. The Journal of Chemical Physics **56**, 13 (1972).

[101] A. B. Anton and D. C. Cadogan. Surface Science **239**, L548 (1990).

[102] L. K. Verheij and M. B. Hugenschmidt. Surface Science **416** (1998).

[103] T. Wahnström, E. Fridell, S. Ljungström, B. Hellsing, B. Kasemo, and A. Rosén. Surface Science **223**, L905 (1989).

[104] P. A. Thiel and T. E. Madey. Surface Science Reports **7**, 211 (1987).

[105] K. M. Backstrand, M. A. Weibel, R. M. Moision, and T. J. Curtiss. The Journal of Chemical Physics **112**, 7209 (2000).

[106] W. M. Haynes (editor). *CRC Handbook of Chemistry & Physics 95:th edition. (online version)*. Taylor and Francis Group, LLC (2014-2015).

[107] S. J. Gentry, J. G. Firth, and A. Jones. Journal of the Chemical Society-Faraday transactions **70**, 600 (1974).

[108] F. V. Hanson and M. Boudart. Journal of Catalysis **53**, 56 (1978).

[109] W. A. de Heer. *Metal Clusters at Surfaces:Structure, Quantum Properties, Physical chemistry*, chapter Confinement and Size Effects in Free Metal Clusters. Springer Verlag (2000).

[110] U. Kreibig and M. Vollmer. *Optical Properties of Metal Clusters*. Springer-Verlag (1995).

[111] G. Mie. Annalen der Physik **25**, 377 (1908).

[112] R. Lazzari, S. Roux, I. Simonsen, J. Jupille, D. Bedeaux, and J. Vlieger. Physical Review B **65**, 235424 (2002).

[113] A. Iline, M. Simon, F. Stietz, and F. Träger. Surface Science **436**, 51 (1999).

[114] H.-M. Benia, N. Nilius, and H.-J. Freund. Surface Science **600**, L128 (2006).

[115] L. Gunnarsson, T. Rindzevicius, J. Prikulis, B. Kasemo, M. Käll, S. Zou, and G. C. Schatz. The Journal of Physical Chemistry B **109**, 1079 (2005).

[116] T. J. Antosiewicz, S. P. Apell, M. Zäch, I. Zorić, and C. Langhammer. Physical Review Letters **109**, 247401 (2012).

[117] W. Hoheisel, K. Jungmann, M. Vollmer, R. Weidenauer, and F. Träger. Physical Review Letters **60**, 1649 (1988).

[118] K. Watanabe, D. Menzel, N. Nilius, and H.-J. Freund. Chemical Reviews **106**, 4301 (2006).

[119] C. Langhammer, Z. Yuan, I. Zorić, and B. Kasemo. Nano Letters **6**, 833 (2006).

[120] N. Nilius, N. Ernst, and H.-J. Freund. Chemical Physics Letters **349**, 351 (2001).

[121] D. Mulugeta, K. H. Kim, K. Watanabe, D. Menzel, and H.-J. Freund. Physical Review Letters **101**, 146103 (2008).

[122] K. M. Mayer and J. H. Hafner. Chemical Reviews **111**, 3828 (2011).

[123] L. Österlund. *Elementary Surface Processes on Graphite and Aluminium*. Ph.D. thesis, Department of Applied Physics, Chalmers University of Technology and Göteborg University, Göteborg, Sweden (1997).

[124] H. Ibach. *Physics of Surfaces and Interfaces*, chapter Basic Techniques. Springer-Verlag Berlin Heidelberg (2006).

[125] H. Ibach and D. L. Mills. *Electron Energy Loss Spectroscopy and Surface Vibrations*. Academic Press Inc. New York (1982).

[126] J. Demuth and H. Ibach. Surface Science **85**, 365 (1979).

[127] R. Greenler. In *Vibrations at Surfaces* (1982).

[128] H. Ibach. Surface Science **299/300**, 116 (1994).

[129] D. A. King. Surface Science **47**, 384 (1975).

[130] P. A. Redhead. Vacuum **12**, 203 (1962).

[131] H. Fredriksson, Y. Alaverdyan, A. Dmitriev, C. Langhammer, D. Sutherland, M. Zäch, and B. Kasemo. Advanced Materials **19**, 4297 (2007).

[132] A. W. Grant, Q.-H. Hu, and B. Kasemo. Nanotechnology **15**, 1175 (2004).

[133] S. Kunz, K. Hartl, M. Nesselberger, F. F. Schweinberger, G. Kwon, M. Hanzlik, K. J. J. Mayrhofer, U. Heiz, and M. Arenz. Physical Chemistry Chemical Physics **12**, 10288 (2010).

[134] U. Heiz, F. Vanolli, L. Trento, and W.-D. Schneider. Review of Scientific Instruments **68**, 1986 (1997).

[135] F. F. Schweinberger. *Catalysis with Supported Size-selected Pt Clusters: Fundamental UHV and Applied Ambient Experiments*. Ph.D. thesis (2014).

[136] C. Langhammer, E. M. Larsson, B. Kasemo, and I. Zorić. Nano Letters **10**, 3529 (2010).

[137] The SEM-picture was taken by Pooya Tabib Zadeh Adibi.

[138] O. Yeshchenko, I. Bondarchuk, V. Gurin, I. Dmitruk, and A. Kotko. Surface Science **608**, 275 (2013).

[139] E. M. Larsson, J. Millet, S. Gustafsson, M. Skoglundh, V. P. Zhdanov, and C. Langhammer. ACS Catalysis **2**, 238 (2012).

[140] S. K. So, R. Franchy, and W. Ho. The Journal of Chemical Physics **95**, 1385 (1991).

[141] J. Bosbach, D. Martin, F. Stietz, T.Wenzel, and F. Träger. Applied Physics Letters **74**, 2605 (1999).